

Chapter 6

Discussion and Conclusion

The application of high-frequency seismograms to damage detection in civil structures was investigated. Two novel methods for SHM were developed and validated using small-scale experimental testing, existing structures *in situ*, and numerical testing.

The first method is developed for pre-Northridge steel-moment-resisting frame buildings that are susceptible to weld fracture at beam-column connections. The method is based on using the response of a structure to a nondestructive force (i.e., a hammer blow) to approximate the response of the structure to a damage event (i.e., weld fracture). In Chapter 2, the method was applied to a small-scale experimental frame, where the impulse response functions of the frame were generated during an impact hammer test. In Chapter 4, the method was applied to a numerical model of a steel frame, in which weld fracture was modeled as the tensile opening of a Mode I crack. Impulse response functions were experimentally obtained for a steel moment-resisting frame building *in situ*. Results indicated that while acceleration and velocity records generated by a damage event are best approximated by the acceleration and velocity records generated by a colocated hammer blow, the method may not be robust to noise. The method seems to be better suited to damage localization, where information such as arrival times and peak accelerations can also provide indication of the damage location. This is of significance for sparsely-instrumented civil structures.

The second SHM method is designed to extract features from high-frequency acceleration records that may indicate the presence of damage. As short-duration high-frequency signals (i.e., pulses) were observed to be indicative of damage, the method relies on the

identification and classification of pulses in the acceleration records. Briefly, pulses observed in the acceleration time series when the structure is known to be in an undamaged state are compared with pulses observed when the structure is in a potentially damaged state. By comparing the pulse signatures from these two situations, changes in the high-frequency dynamic behavior of the structure can be identified, and damage signals can be extracted and subjected to further analysis. It is recommended that, in practice, the method be combined with a vibration-based method that can be used to estimate the loss of stiffness. In Chapter 3, the method was successfully applied to a small-scale experimental shear beam that was dynamically excited at its base using a shake table and damaged by loosening a screw to create a moving part. Although the damage was observed to be aperiodic and non-linear in nature, the damage signals were accurately identified, and the location of damage was determined using the amplitudes and arrival times of the damage signal. In Chapter 5, the method was also successfully applied to detect the occurrence of damage in a test bed data set provided by the Los Alamos National Laboratory, in which nonlinear damage was introduced into a small-scale steel frame by installing a bumper mechanism that inhibited the amount of motion between two floors. The method was successfully applied and was robust despite a low sampling rate, though false negatives (undetected damage signals) were observed to occur at high levels of damage when the frequency of damage events increased. The method was also applied to acceleration data recorded on a damaged cable-stayed bridge in China, provided by the Center of Structural Monitoring and Control at the Harbin Institute of Technology. Acceleration records recorded after the date of damage showed a clear increase in high-frequency short-duration pulses compared to those previously recorded. One undamage pulse and two damage pulses were identified from the data. The occurrence of the detected damage pulses was consistent with a progression of damage and matched the known chronology of damage. The damage pulse originated between the end of the bridge and the first accelerometer; damage may have occurred within this region.

The findings of each chapter are repeated below.

Chapter 2: Experimental Study: Damage Detection Method for Weld Fracture of Beam-Column Connections in Steel Moment-Resisting-Frame Buildings

An experimental study was conducted to provide insight into a damage detection method that makes use of a prerecorded catalog of IRF templates and a cross-correlation method to detect the occurrence and location of structural damage in an instrumented building. Impulsive hammer blows and bolt fracture were applied to a small-scale steel frame to test the feasibility of applying the method to a building. The similarity between structure responses was evaluated using a cross-correlation method. The main findings of this chapter are:

1. IRFs were successfully obtained for an existing steel moment-resisting-frame building *in situ*. Not only were the IRFs clearly observable over ambient noise, the waveforms were also very consistent between trials with colocated sources, with correlation values typically greater than 0.8. For IRFs generated by hammer blows at different locations, significant differences were observed in arrival times, peak accelerations, and waveforms using eight accelerometers recording at 100 kHz. The data supports the idea of using hammer blow data to localize damage to a single column within a story. A sampling rate of 100 sps, though preferably 500 sps, seems to be high enough to capture the IRFs in the Factor building.
2. The application of the proposed damage detection method to the small-scale frame suggests that the IRF is not a robust approximation of the response to bolt failure. The method may also be suitable for damage localization, especially if it is combined with information about the arrival times and peak accelerations. While the IRFs cross-correlated well with each other and the responses to bolt fracture cross-correlated well with each other when the sources were colocated, the IRFs and responses to bolt fracture did not. However, in all considered cases, the IRF that had the highest correlation value with the response of the frame to bolt failure was the colocated IRF. Improvements in the correlation values were made by using an amplitude-dependent normalization that scaled with the maximum amplitude of acceleration at each receiver in response to bolt fracture. Information, such as arrival times and peak accelerations,

can also be indicators of where damage occurred; this is of significance for sparsely-instrumented structures.

3. The response of the frame to bolt fracture was observed to be surprisingly consistent between trials (correlation values of 0.70-0.85 for responses with colocated sources). This suggests that the mechanism that occurs at the moment of bolt failure is consistent between trials, and a hammer blow does not well-characterize this source. This also implicates that if a building were to undergo damage that resulted in the creation of a repeating source, a repeating high-frequency, short-duration signal might be observed in the acceleration time series. This could be generated by damage cases such as in the case of a breathing crack that repeatedly opens and closes, or a change in boundary conditions that increases the flexibility of a member and allows for the excitation of traveling waves.
4. The pre-recorded IRFs differed significantly from the IRFs that were recorded when the frame was in a damaged state, with typical cross-correlation values of 0.5, as compared to pre-damage values of 0.8. By comparing the generation of waves propagating through the frame, it was seen that the response of the damaged structure to a hammer blow applied at a given location begins to diverge from the response of the undamaged structure only after the elastic waves recorded at a given receiver location passed through the region of damage. This phenomenon is similar to the guided wave methods used in acoustic damage detection methods, and it also has potential to be used for damage detection in larger-scale structures. It would be necessary to use a repeatable mechanism to excite the structure over time, preferably under similar environmental conditions, and differences between the baseline signal and the subsequent recorded signal would be used to indicate damage. Damage might be located through an inverse problem approach that makes use of a finite-element model.
5. The application of a hammer blow to a damaged connection resulted in a low correlation value with the pre-recorded IRF generated by a colocated hammer blow. In this case,

the damaged connection was observed to also act as a high-frequency source, most likely due to motion generated at the interface of the beam and column. Applying a hammer blow to a cracked beam or column in a real building may or may not result in high-frequency energy generated at the crack interface. Presumably, if a beam has a crack and the two sides of the crack are not held firmly together, e.g., a vertical crack in a beam, a hammer blow applied in the vicinity of the crack could result in mechanical slippage and impact caused by the relative motion at the crack interface. If, on the other hand, the crack is firmly held closed, as might be the case for a horizontal crack in a column, high-frequency energy might not be generated at the crack interface in response to a nearby hammer blow.

6. As the responses to bolt fracture correlated just as well with pre-recorded IRFs as they did with the post-damage IRFs, it may be desirable to record the IRFs after an earthquake has occurred, when the building is in a potentially damaged state. In this way, there is an additional chance of detecting any high-frequency energy that is generated within a cracked interface at a damaged connection. (Also, if the building is never subjected to a large earthquake, there will be no need to conduct the hammer blow trials in the first place.) One advantage of having previously-recorded IRFs, however, is that they can be directly compared with post-earthquake IRFs, in order to detect damage in the frame by differences between them.

Chapter 3: Experimental Shear Beam

The effect of damage on the dynamic response of a civil structure was investigated experimentally using a small-scale (0.75 meter tall) shear beam. Damage was introduced into the shear beam by loosening the bolts connecting the columns to the floor, and a shake table was used to apply a consistent pulse at the base of the beam. The main findings of this chapter are outlined below:

1. A dynamic pulse was input at the base of the shake table. High-frequency acceleration records could be used to immediately determine the presence and location of damage,

based on the presence of short-duration high-frequency signals caused by mechanical impact and slippage. Low-frequency acceleration records could also be used to immediately determine the location of damage (i.e., which floor), based on the delayed arrival times and amplitudes of the initial shear wave.

2. A damage detection method that is based on detecting pulses in both the undamaged and potentially damaged acceleration records was found to be successful in detecting the nonlinear, aperiodic occurrences of damage signals. The arrival times and amplitudes were used to determine which floor was damaged. The advantage this strategy has over current strategies is that it can detect early onset damage. It is also based on the physical mechanism of damage in the structure, namely wave propagation, and energy formulations or the combination of the method with a time-reversed reciprocal method could give more information about the damage mechanism. The obvious disadvantage is that if there are no pulses (due not using a high-enough sampling rate, or the absence of such a signal), the method will not work. Another disadvantage is that the method cannot be used to determine the amount of damage (e.g., loss of stiffness), it can only detect the occurrence of signals that may indicate damage. The method could be combined with a vibration-based method.
3. A static tilt test was performed to estimate the severity of damage for Levels 1, 2, and 3. The amount of damage was found to range from moderate to severe levels, with estimated stiffness parameter k_a/d_{ud} ranging from 0.27 to 0.74. The estimated shear wave speeds obtained during dynamic testing were used to quantify the amount of damage, and the level of damage was estimated to be less severe than the values obtained from the stiffness test. The mean values (and standard deviations) of the estimated inter-story lateral stiffnesses immediately beneath the damaged floor for Damage Levels 1, 2, and 3, respectively, were found to be 0.93 (0.03), 0.70 (0.1), and 0.82 (0.23). The mean values (and standard deviations) of the estimated inter-story lateral stiffness immediately above the damaged floor for Damage Levels 1, 2, and 3, respectively, were found to be 0.94 (0.03), 0.67 (0.09), and 0.80 (0.24). The mean

values (and standard deviations) of the estimated inter-story lateral stiffness in floors not immediately above or below the damaged floor were calculated to be 0.99 (0.03), 0.95 (0.07), and 0.96 (0.05). The dynamic estimates could be improved by considering a longer portion of the time series. The values could be tested using forward modeling by determining the accompanying natural frequencies and mode shapes and comparing those with the observed ones.

4. The modal response of the structure was found to be highly consistent between trials, though the introduction of damage results in the presence of transient signals that generally originate at the damaged floor. A decreased transmission through the damaged floor of the high-frequency motion generated by the shake table was also observed.

Chapter 4: Numerical Study: Time-Reversed Reciprocal Method and Damage Detection Method for Weld Fracture

To numerically test a method for damage detection, a steel frame's response to two loading cases, an impulse-like force and an opening crack tensile stress (Mode I crack), was computed on a temporal scale of microseconds. It was found that the velocity waveform of a tensile crack can be approximated by the velocity waveform of an impulse-like force applied at the same beam-column connection of a steel frame. The results support the use of waveform cross-correlation using a pre-event catalog of impulse response function templates to determine the location and time of occurrence of a subsequent fracture recorded on a network of vibration sensors. However, the damage detection method may not be robust in a real setting, and the method may be better suited for damage localization.

A time-reversed reciprocal method was applied to a two-story one-bay numerical steel frame, as a proof of concept for applying the methodology to a complex structure such as a bridge or building. The signal was not fully recovered, but the location and application time of the impulse-like force were successfully determined. In applying this method to an actual structure, an accurate numerical model would first need to be developed for the structure in the frequency range of interest, which could be both challenging and computationally-

expensive. Once a satisfactory numerical model is obtained, the experimental data, which would contain some elements of noise, would be time-reversed and input to the model at the original receiver locations. It would be interesting to see this method applied to a full-scale experimental structure.

Chapter 5: Application of High-Frequency Damage Detection Methods to Benchmark Problems

The presence of high-frequency short-duration signals in the acceleration records were observed to indicate damage in two benchmark problems, the LANL nonlinear frame and the SMC damaged cable-stayed bridge. In each example, the damage signals were successfully isolated by applying a method to identify potential damage signals through feature extraction of pulses. The method effectively uses the matched filter method to detect the occurrence of repeating signals, and identify new pulses that could indicate damage.

In the LANL nonlinear frame example, the damage signal took the form of elastic waves generated by the impact of a bumper mechanism. By using either high-pass filtering or a time-frequency representation, the damage signal could be clearly detected as high-frequency pulses in the acceleration records obtained on the two floors housing the bumper mechanism. The method was observed to be robust despite the low sampling rate, though an increase in false negatives was observed. Additional false negatives occur at high levels of damage when there was little time separation between damage signals. However, the damage signal was successfully isolated, and it was possible to localize the damage, based on the amplitudes of the damage signals, to the top two floors of the structure.

Acceleration data was obtained from a damaged cable-stayed bridge in China. An increase in high-frequency short-duration pulses is clearly observed in the acceleration records, and the occurrence of these pulses alone might be used to indicate the presence of damage. An abrupt decrease in acceleration levels that was caused by preventative measures taken to limit traffic to prevent the collapse of the bridge indicated that the pulses are primarily caused by traffic. One undamage (T_1^{UD}) and two damage signals (T_1^D and T_2^D) were isolated using the feature extraction method. Damage signal T_1^D appears to be generated by vehicle

loading on the south end of the bridge; signals T_1^{UD} and T_2^D seem to have been generated by the same source mechanism and location, namely vehicle loading on the north end of the bridge. All acceleration data (recorded during the same time period during light traffic) was screened for the presence of the undamage and damage signals using a threshold value of 0.35. The undamage signal was detected multiple times in each dataset. The damage signals were first detected in the March 30 acceleration record, and they were also detected multiple times in all subsequent records. This is consistent with the occurrence of damage signal T_1^D indicating the progression of damage, and the change in the undamage signal T_1^{UD} indicating a progression of damage. Assuming similar traffic loads were encountered on different days at the same local time, it seems that when the bridge was in an undamaged state, a few (presumably heavy) vehicles excited a large dynamic response in the structure. When damage occurred in the bridge, a change in the physical properties of the bridge occurred that resulted in the ability of most vehicles to excite a large dynamic response in the structure, presumably due to an increase in flexibility. If the observed traveling wave is generated by the rapid loading event that occurs as a vehicle drives onto a region of increased flexibility on the bridge, this would indicate that the damage location is located between each outside sensor and the closest end of the bridge (i.e., between the south end of the bridge and the first sensor, and between the north end of the bridge and the fourteenth sensor). Additional analysis would be needed to determine if the increased flexibility is caused by damage to the stay cables, bridge girders, or other reasons. Low-frequency strain data recorded on the cable stays could be used to assess cable damage. It would be advantageous to combine this method with a traditional vibration method, as decreases in natural frequencies were observed.

There is some art in choosing the threshold value; too high a threshold value will result in false negatives (missed detections), and too low a threshold value will result in false positives. It might be possible to determine an optimal threshold value by actively exciting the structure using a few known sources (i.e. hammer blow or a known car of a given speed) over the course of a few weeks and experimentally determining an appropriate range based on the analysis of the method using the known signals.

There is also some art in choosing the filtering threshold. It is relatively easier to do this for simple experimental models that are excited along a single axis – a cut-off frequency above the predominant modal frequencies of the structure is desired, and the number of modes to consider is approximately given by the number of floors. For full-scale structures *in situ*, different modes are excited during different environmental conditions, and numerical models typically have a larger number of modes than are excited in the real structure. Model reduction can be used to estimate the highest mode present in the real structure and hence the highest mode above which to filter. Finally, some consideration must be given to the frequency content of the damage signal. Different frequencies are expected to be emitted for different damage mechanisms (e.g. acoustic emission, mechanical impact, generation of a flexural wave).

Finally, while applying the feature detection method can successfully isolate the damage signal in the case of known damage to a structure with a baseline recording, the ability of the technique to quantitatively determine the severity of damage (i.e., loss in stiffness or increase in flexibility), and hence to definitively determine the presence of damage, is lacking. Changes in the dynamic behavior of the structure can be identified using outlier methods, changes in damage severity can be determined qualitatively, and the damage signal can be used to determine where damage occurred and give an energy estimate, but the damage signal cannot on its own be used to determine the loss in stiffness of the structure, and hence should be combined with knowledge of the structure (e.g., a finite-element model with knowledge of potential damage locations and mechanisms), a statistical approach using data recorded on multiple damaged structures of a similar type (these data would need to be experimentally obtained), or a complementary vibration-based damage detection method.

Appendix A

Appendix

A.1 Notation, Definitions, and Properties

These properties were found in Bracewell (1986).

Cross-correlation:

$$\begin{aligned}(x_n \star x_m)(t) &= \int_{-\infty}^{\infty} \overline{x_n(\tau)} x_m(t + \tau) d\tau, \\ (x_n \star x_m)[p] &= \sum_{q=-\infty}^{\infty} \overline{x_n[q]} x_m[p + q].\end{aligned}$$

Convolution:

$$\begin{aligned}(x_n * x_m)(t) &= \int_{-\infty}^{\infty} x_n(\tau) x_m(t - \tau) d\tau, \\ (x_n * x_m)[p] &= \sum_{q=-\infty}^{\infty} x_n[q] x_m[p - q].\end{aligned}$$

Fourier Transform and Inverse Fourier Transform:

$$\begin{aligned}\hat{x}_n(\xi) &= \mathcal{F}\{x_n(t)\} = \int_{-\infty}^{\infty} x_n(t)e^{-2\pi i t \xi} dt, \\ x_n(t) &= \mathcal{F}^{-1}\{\hat{x}_n(\xi)\} = \int_{-\infty}^{\infty} \hat{x}_n(\xi)e^{2\pi i t \xi} d\xi, \\ \hat{x}_n(\omega) &= \mathcal{F}\{x_n(t)\} = \frac{1}{\sqrt{2\pi}} \int_{-\infty}^{\infty} x_n(t)e^{-i\omega t} dt, \\ x_n(t) &= \mathcal{F}^{-1}\{\hat{x}_n(\omega)\} = \frac{1}{\sqrt{2\pi}} \int_{-\infty}^{\infty} \hat{x}_n(\omega)e^{i\omega t} d\omega, \\ X_n[p] &= \sum_{q=0}^{N-1} x_n[q]e^{-2\pi i p q/N}, \\ x_n[q] &= \frac{1}{N} \sum_{p=0}^{N-1} X_n[p]e^{2\pi i p q/N}.\end{aligned}$$

Laplace Transform and Fourier Transform:

$$\begin{aligned}\mathcal{L}\{x_n(t)\} &= X_n(s) = \int_0^{\infty} x_n(t)e^{-st} dt, \\ \mathcal{L}^{-1}\{X_n(s)\} &= x_n(t) = \frac{1}{2\pi i} \lim_{T \rightarrow \infty} \int_{\gamma-iT}^{\gamma+iT} X_n(s)e^{st} ds, \\ X_n(s)|_{s=i\omega} &= \mathcal{F}\{x_n(t)\}, \\ s &= \sigma + i\omega.\end{aligned}$$

Fourier Transform of Cross-correlation:

$$\mathcal{F}\{x_n \star x_m\} = \overline{\mathcal{F}\{x_n\}} \mathcal{F}\{x_m\}.$$

Fourier Transform of Convolution:

$$\mathcal{F}\{x_n * x_m\} = \mathcal{F}\{x_n\} \mathcal{F}\{x_m\}.$$

Properties of Convolution and Cross-correlation:

$$\begin{aligned}
 x_n * (x_m + x_p) &= (x_n * x_m) + (x_n * x_p), \\
 x_n * x_m &= x_m * x_n, \\
 x_n * (x_m * x_p) &= (x_n * x_m) * x_p, \\
 x_n * \delta &= x_n, \\
 \frac{d}{dt}(x_n * x_m) &= \frac{dx_n}{dt} * x_m = x_n * \frac{dx_m}{dt}, \\
 x_n \star x_m &= \overline{x_n(-)} * x_m, \\
 (x_n * x_m) \star x_p &= x_m(-) * (x_n \star x_p).
 \end{aligned}$$

where $x_n(-) = x_n(-t)$ denotes the time-reversed $x_n(t)$, and $\overline{x_n} = \overline{x_n(t)}$ denotes the complex conjugate of $x_n(t)$.

A.2 Publications

Heckman, V. M., Kohler, M. D., and Heaton, T. H. (2011b). A method to detect structural damage using high-frequency seismograms. In *Proceedings of Structural Health Monitoring 2011: International Workshop on Structural Health Monitoring*.

Abstract: “There has been recent interest in using acoustic techniques to detect damage in instrumented civil structures. An automated damage detection method that analyzes recorded data has application to building types that are susceptible to a signature type of failure, where locations of potential structural damage are known a priori. In particular, this method has application to the detection of brittle fractures in welded beam-column connections in steel moment-resisting frames (MRFs). Such a method would be valuable if it could be used to detect types of damage that are otherwise difficult and costly to identify. The method makes use of a prerecorded catalog of Greens function templates and a matched filter method to detect the occurrence and location of structural damage in an in-

strumented building. This technique is different from existing acoustic methods because it is designed to recognize and use seismic waves radiated by the original brittle failure event where the event is not known to have occurred with certainty and the resulting damage may not be visible. The method is outlined as follows. First, identify probable locations of failure in an undamaged building. In pre-Northridge steel MRFs, which are susceptible to brittle failure of welded beam-column connections, those connections would be the locations of probable failure for this type of building. Second, obtain a Greens function template for each identified location of probable failure by applying a short-duration high-frequency pulse (e.g. using a force transducer hammer) at that location. One underlying assumption of this method is that the Greens function template specific to a potential location of failure can be used to approximate the dynamic response of the structure to structural damage at that location. Lastly, after a seismic event, systematically screen the recorded high-frequency seismograms for the presence of waveform similarities to each of the catalogued Greens function templates in order to detect structural damage. This is achieved by performing a running cross-correlation between each Greens function template and a moving window of the continuous data recorded during the earthquake. Damage that occurs at one of the catalogued potential locations is expected to result in a high cross-correlation value when using the correct Greens function template. This method, also known as the matched filter method, has seen recent success in other fields, but has yet to be explored in the context of acoustic damage detection in civil structures. Preliminary experimental results from tap tests performed on a small-scale laboratory frame are presented. Cross-correlation calculations highlight similarities among events generated at the same source location and expose differences among events generated at different source locations. Finally, a blind tap test is performed to test whether cross-correlation techniques and catalogued Greens function templates can be used to identify the occurrence of and pinpoint the location of an assumed-unknown event (Heckman et al., 2011b).”

Heckman, V., Kohler, M., and Heaton, T. (2011a). A damage detection method for instrumented civil structures using prerecorded greens functions and cross-correlation. In

Abstract: “Automated damage detection methods have application to instrumented structures that are susceptible to types of damage that are difficult or costly to detect. The presented method has application to the detection of brittle fracture of welded beam-column connections in steel moment-resisting frames (MRFs), where locations of potential structural damage are known a priori. The method makes use of a prerecorded catalog of Greens function templates and a cross-correlation method to detect the occurrence, location, and time of structural damage in an instrumented building. Unlike existing methods, the method is designed to recognize and use mechanical waves radiated by the original brittle fracture event, where the event is not known to have occurred with certainty and the resulting damage may not be visible. An experimental study is conducted to provide insight into applying the method to a building. A tap test is performed on a small-scale steel frame to test whether cross-correlation techniques and catalogued Greens function templates can be used to identify the occurrence and location of an assumed-unknown event. Results support the idea of using a nondestructive force to characterize the building response to high-frequency dynamic failure such as weld fracture (Heckman et al., 2011a).”

Heckman, V. M., Kohler, M. D., and Heaton, T. H. (2011c). A method to detect structural damage using high-frequency seismograms. In *Proceedings of the 8th International Conference on Urban Earthquake Engineering*.

Abstract: “A numerical study is performed to gain insight into applying a novel method to detect high-frequency dynamic failure in buildings. The method relies on prerecorded catalog of Green’s functions for instrumented buildings. Structural failure during a seismic event is detected by screening continuous data for the presence of waveform similarities to each of the cataloged building responses. In the first part of this numerical study, an impulse-like force is applied to a beam column connection in a linear elastic steel frame. A time-reversed

reciprocal method is used to demonstrate that the resulting simulated displacements can be used to determine the absolute time and location of the applied force. In the second part of the study, a steel frame’s response to two loading cases, an impulse-like force and an opening crack tensile stress, is computed on a temporal scale of microseconds. Results indicate that the velocity waveform generated by a tensile crack can be approximated by the velocity waveform generated by an impulse-like force load applied at the proper location. These results support the idea of using a nondestructive impulse-like force (e.g. hammer blow) to characterize the building response to high-frequency dynamic failure (e.g. weld fracture) (Heckman et al., 2011c).”

Heckman, V., Kohler, M., and Heaton, T. (2010). Detecting failure events in buildings: A numerical and experimental analysis. In *Proceedings of the 9th U.S. National 10th Canadian Conference on Earthquake Engineering. Earthquake Engineering Research Institute.*

Abstract: “A numerical method is used to investigate an approach for detecting the brittle fracture of welds associated with beam-column connections in instrumented buildings in real time through the use of time-reversed Greens functions and wave propagation reciprocity. The approach makes use of a prerecorded catalog of Greens functions for an instrumented building to detect failure events in the building during a later seismic event by screening continuous data for the presence of waveform similarities to one of the prerecorded events. This study addresses whether a set of Greens functions in response to an impulsive force load can be used to approximate the response of the structure to a localized failure event such as a brittle weld fracture. Specifically, we investigate whether prerecorded Greens functions can be used to determine the absolute time and location of a localized failure event in a building. We also seek to differentiate between sources such as a weld fracture that are structurally damaging and sources such as falling or colliding furniture and other non-structural elements that do not contribute to structural failure. This is explored numerically by comparing the dynamic response of a finite-element cantilevered beam model

structure to a variety of loading mechanisms. A finite-element method is employed to determine the behavior of the resulting elastic waves and to obtain a general understanding of the structural response (Heckman et al., 2010).”

Kohler, M. D., Heaton, T. H., and Heckman, V. M. (2009). A time-reversed reciprocal method for detecting high-frequency events in civil structures with accelerometer arrays. *In Proceedings of ANCRISST 2009 - The Fifth International Workshop on Advanced Smart Structures and Technology.*

Abstract: “A high-frequency experimental method of detecting a failure event in engineered structures is presented that uses the property of wave propagation reciprocity and time-reversed reciprocal Greens functions. The premise is that if a numerical database of pre-event, source-receiver Greens functions can be compiled for multiple locations of potential damage in a structure, that database can subsequently be used to identify the location and time of occurrence of a real failure event in the structure. Once a fracture source emits a wavefield that is recorded on a distributed set of accelerometers in the structure, time-reversed waves can be obtained by convolving the displacements with the database of time-reversed Greens functions and stacking the results. The correct location and time of the fracture source can be inferred from the subset of Greens functions that exhibits the best focus in the form of a delta function. The 17-story, steel moment-frame UCLA Factor building contains a cutting-edge, continuously recording, 72-channel, seismic array. The accelerometers 500 sample-per-second recordings have been used to verify the ability to observe impulse-like sources in a full-scale structure. Application of an impulse-like source on the 3rd and 15th floors of the Factor building shows that the associated displacements serve as useful approximations to the buildings Greens functions in the far field, and can be used in investigations of scenario fracture location and timing (Kohler et al., 2009).”

A.3 Uniform Shear Beam

Consider a simple undamped shear beam model that is fixed at the base with a height $H = 100$ m, shear wave velocity $\beta = 200$ m/s, and with sensors located at each 1/10 of the height of the building recording at 100 sps. The shear wave velocity, β , is proportional to the square root of the stiffness, $\beta = \sqrt{\mu/\rho}$, where μ is the interstory shear modulus, and ρ is the density. The beam is subjected to displacement at the base, $u_0(t)$,

$$\begin{aligned}\frac{\partial^2 u}{\partial t^2} &= \beta^2 \frac{\partial^2 u}{\partial x^2}, \\ u &= u(x, t), \\ u(0, t) &= u_0(t), \\ \frac{\partial u}{\partial x}(H, t) &= 0.\end{aligned}$$

Its solution at the n^{th} floor is given by the D'Alembert solution to the wave equation with fixed-free boundary conditions (Sasani et al., 2006). The horizontal ground motion generates a vertically propagating shear wave. The fixed-base period, T , is $4H/c$. The building motion consists of a sum of upgoing and downgoing waves, and is given by:

$$\begin{aligned}u_n(t) = u_0\left(t - \frac{nT}{40}\right) - u_0(t) + \sum_{m=1}^{2t/T+n/20} (-1)^{m+1} u_0\left(t - \frac{(2m - n/10)T}{4}\right) \\ + \sum_{m=1}^{2t/T-n/20} (-1)^{m+1} u_0\left(t - \frac{(2m + n/10)T}{4}\right).\end{aligned}\tag{A.1}$$

Using this model, one can directly compare the response of the shear beam from applying an impulsive displacement at the base to the impulse response (with simulated noise applied at the base) and cross-correlations (with simulated noise applied at the base), as shown in Figure A.1. To simulate ambient noise at the base of the shear beam, displacements are drawn from a uniform distribution over the range $[-0.05, 0.05]$ meters. Results have been stacked over 10 trials.

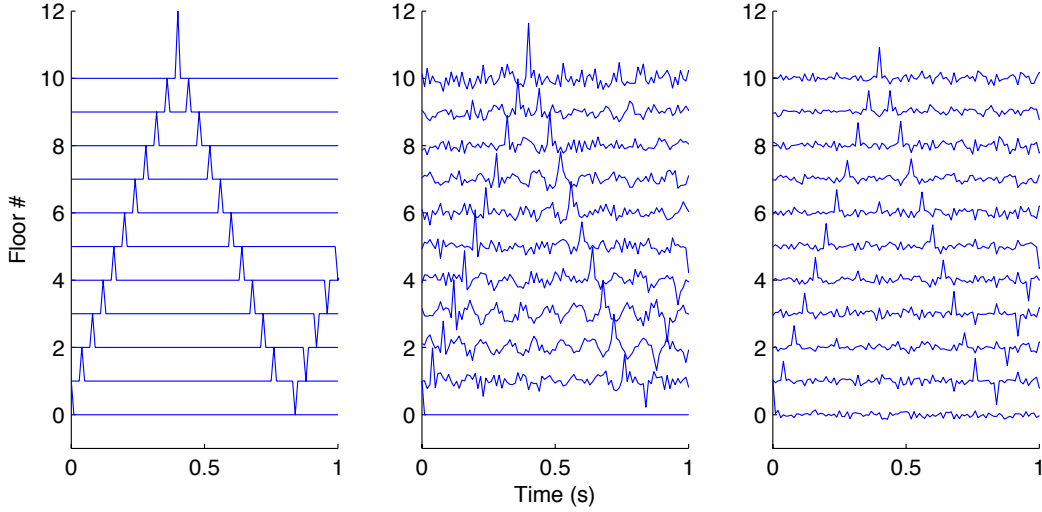


Figure A.1: **Simple Shear Beam Synthetics.** **A**, An impulsive shear wave travels up the simple shear beam, is reflected at the top floor, and is reflected again at the fixed base. **B**, Deconvolution is used to obtain the impulse response function from synthetic ambient noise motion at the base. **C**, Normalized cross-correlation is performed between each record and the base record under ambient noise conditions.

The natural frequencies are:

$$\omega_n = \frac{(2n - 1)\pi\beta}{2H}; n = 1, 2, 3, \dots \quad (\text{A.2})$$

If an interface is introduced into the shear beam at height $H_{interface}$, so that there are now two separate regions A and B, then the differential equations governing the motion of the beam are as follows:

Region A: $0 \leq x_3 \leq H_{interface}$,

$$\begin{aligned} \frac{\partial^2 u_A}{\partial t^2} &= \beta_A^2 \frac{\partial^2 u_A}{\partial x^2}, \\ u_A &= u_A(x_3, t), \\ u_A(0, t) &= u_0(t). \end{aligned}$$

Region B: $H_{interface} \leq x_3 \leq H$,

$$\begin{aligned}\frac{\partial^2 u_B}{\partial t^2} &= \beta_B^2 \frac{\partial^2 u_B}{\partial x^2}, \\ u_B &= u_B(x_3, t), \\ \frac{\partial u_B}{\partial x}(H, t) &= 0.\end{aligned}$$

Interface:

$$\begin{aligned}u_B(H_{interface}, t) &= u_B(H_{interface}, t), \\ \frac{\partial u_A}{\partial x}(H_{interface}, t) &= \frac{\partial u_B}{\partial x}(H_{interface}, t).\end{aligned}$$

The reflection and transmission coefficients for a vertically-incident wave generated at the base are:

$$\begin{aligned}T &= \frac{A_T}{A_I} = \frac{2}{1 + \beta_2/\beta_1}, \\ R &= \frac{A_R}{A_I} = \frac{\beta_1/\beta_2 - 1}{\beta_1/\beta_2 + 1}.\end{aligned}$$

A schematic for wave propagation in a shear beam, presented for a variety of boundary conditions, is given in Figure A.2.

The transmission and reflection coefficients for an infinite shear beam with a low-velocity

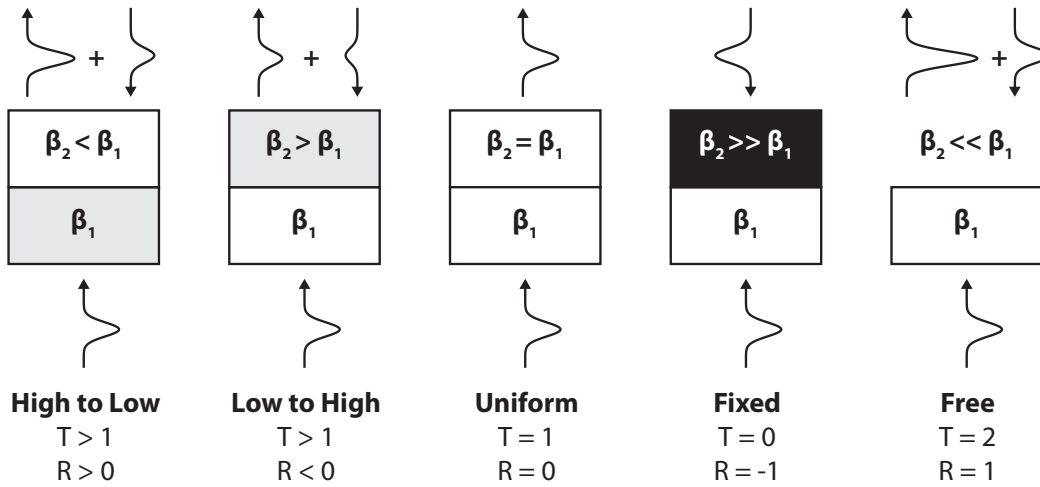


Figure A.2: Wave Propagation in a Shear Beam: Transmission and Reflection Coefficients for a Variety of Boundary Conditions. Wave propagation in a shear beam is presented for a variety of boundary conditions.

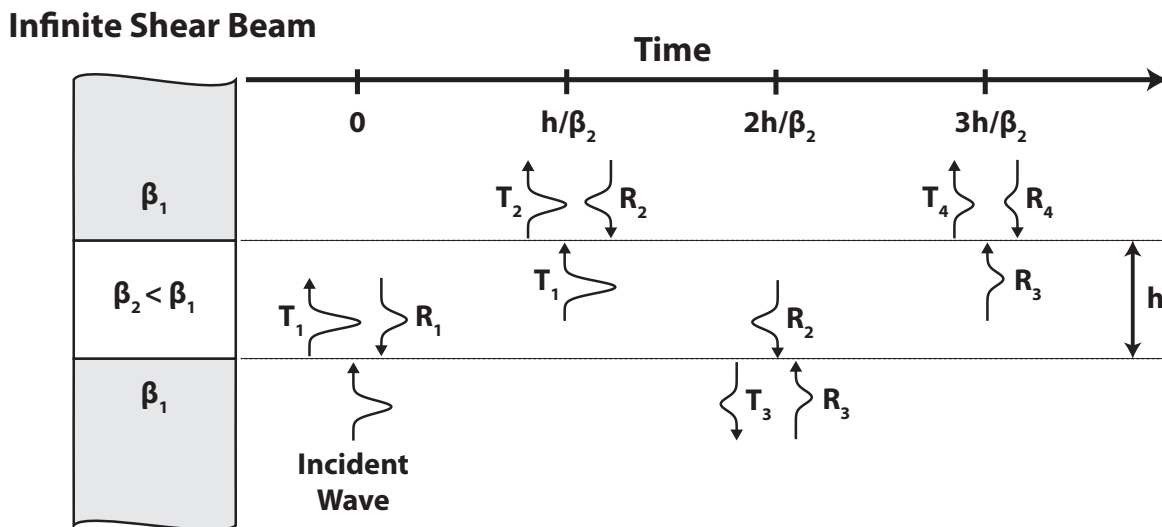


Figure A.3: Wave Propagation in an Infinite Shear Beam with a Low-Velocity Layer. A schematic of the different waves is shown.

layer, shown in Figure A.3, are computed as:

$$\begin{aligned}
T_1 &= A_T/A_I \\
&= \frac{2}{1 + \beta_2/\beta_1}, \\
R_1 &= A_R/A_I \\
&= \frac{\beta_1/\beta_2 - 1}{\beta_1/\beta_2 + 1}, \\
T_2 &= T_1 \frac{2}{1 + \beta_1/\beta_2} \\
&= \frac{2}{1 + \beta_2/\beta_1}, \\
R_2 &= T_1 \frac{\beta_2/\beta_1 - 1}{\beta_2/\beta_1 + 1} \\
&= \frac{2}{1 + \beta_2/\beta_1} \frac{\beta_2/\beta_1 - 1}{\beta_2/\beta_1 + 1}, \\
T_3 &= R_2 \frac{2}{1 + \beta_1/\beta_2} \\
&= \frac{2}{1 + \beta_2/\beta_1} \frac{\beta_2/\beta_1 - 1}{\beta_2/\beta_1 + 1} \frac{2}{1 + \beta_2/\beta_1}, \\
R_3 &= R_2 \frac{\beta_2/\beta_1 - 1}{\beta_2/\beta_1 + 1} \\
&= \frac{2}{1 + \beta_2/\beta_1} \frac{\beta_2/\beta_1 - 1}{\beta_2/\beta_1 + 1} \frac{2}{1 + \beta_2/\beta_1} \frac{\beta_2/\beta_1 - 1}{\beta_2/\beta_1 + 1}, \\
T_n &= R_{n-1} \frac{2}{1 + \beta_1/\beta_2} \\
&= \frac{2}{1 + \beta_2/\beta_1} \frac{\beta_1/\beta_2 - 1}{\beta_2/\beta_1 + 1} \left(\frac{\beta_2/\beta_1 - 1}{\beta_2/\beta_1 + 1} \right)^{n-2}, \\
R_n &= R_{n-1} \frac{\beta_2/\beta_1 - 1}{\beta_2/\beta_1 + 1} \\
&= \frac{2}{1 + \beta_2/\beta_1} \left(\frac{\beta_2/\beta_1 - 1}{\beta_2/\beta_1 + 1} \right)^{n-1}.
\end{aligned}$$

A wave is trapped within the lower velocity layer. It takes the wave h/β_2 seconds to travel through the length h of this layer. The amplitude of the wave changes signs each time

it is reflected, and so the period is equal to $T_{trapped} = \frac{2h}{\beta_2}$, and it decays as $(\frac{\beta_2/\beta_1-1}{\beta_2/\beta_1+1})^2 \frac{\beta_2}{2h}$.

An ongoing shear wave is propagated through an infinite shear beam with a low velocity layer. A series of transmitted and reflected waves are generated. Differences in arrival times and wave amplitudes are observed in the beam with the low velocity layer, compared to a uniform shear beam.

A.4 Application of State Space Method to Acceleration of a High-Rise Building in Osaka

In the dynamic excitation of a structure to a repeating source, the response of the damaged structure does not begin to diverge from the response of the undamaged structure until elastic waves have propagated through the region of damage. Motivated by these findings, the impulse response function of an existing high-rise building in Osaka is generated from the building's response to ambient noise and studied as a means for damage detection.

In dynamically exciting the experimental shear beam studied in Chapter 3, it was observed that the introduction of damage to a single floor of the structure resulted in a slowing of the initial shear wave pulse as it passed through the damaged region, resulting in a clear delay in the arrival time (compared with the arrival time for the undamaged data) on floors above the damaged floor. By using a high sampling rate, the presence and location of damage could be immediately determined, despite the low modal frequencies of the structure (less than 25 Hz) and hence low spatial resolution for damage detection. Motivated by this finding, a numerical study is conducted by introducing damage to a numerical model of an existing high-rise building in the Osaka prefecture. Damage is simulated in the numerical model by reducing the interstory shear stiffness. A horizontal pulse applied at the base of the structure is used as the excitation source. The input pulse at the base of the structure is based on the experimental input pulse obtained by applying correlation methods to the acceleration of the structure during ambient conditions to estimate its IRF. It is found that the low-frequency nature of the noise source generates a broad input pulse that makes damage

detection difficult using this method.

Previous studies have been performed in the context of seismic interferometry of structures. A comparison is made using the simulated IRFs for the damaged and undamaged models. Kohler et al. (2007) deconvolved the subbasement records in UCLA Factor building from upper floor records for 20 earthquakes. The authors developed an ETABS model that agrees with the experimental data. The impulse response function of a building can also be generated using cross-correlation of ambient noise (Prieto et al., 2010). It is common (research) practice in civil engineering to perform modal identification using the cross-correlations of the recorded accelerations of the structure excited by ambient noise (Brincker et al., 2000). Properties of the substructure, such as interstory stiffness, are typically estimated from the modal values.

A.4.1 Experimental Setup

Hayashi et al. (2012) have been monitoring the consecutive vibration characteristics of a high-rise steel building located in the Osaka prefecture. The building, shown in Figures A.4 and A.5, has 21 stories with two stories for the penthouse, and four stories under the ground level. It is a steel moment-resisting frame above ground and a steel-reinforced concrete frame with shear walls under the ground level. It is densely instrumented, with seismometers installed along the center of the structure. Thirteen seismometers (V403BT accelerometers at a sampling interval of 100Hz) are installed on floors B4F and 22F, as well as every other floors from 1F to 21FL. Hayashi et al. have estimated the first three NS natural frequencies to be 0.56 Hz, 1.65 Hz, and 2.97 Hz, and the EW natural frequencies to be 0.56 Hz, 1.65 Hz, 2.91 Hz, from the result of stacking transfer functions recorded for small earthquakes (Hayashi et al., 2012). Impulse responses obtained from earthquake data have been found to be similar to those obtained using microtremor data. The current design analysis models are a multistory shear model and flexure shear model.

The Osaka high-rise building is modeled as a lumped mass system, as shown in Figure A.5. The design parameters were used by Satow Engineers to compute the effective masses



Figure A.4: **Osaka High-Rise: Photo of the Building.** The building, shown in Figures A.4 and A.5, has 21 stories with two stories for the penthouse, and four stories under the ground level. It is a steel moment-resisting frame above ground and a steel-reinforced concrete frame with shear walls under the ground level.

and stiffnesses; they are listed in Table A.6 along with the accompanying floor names and heights (Satow, 1962). The motion of the model is constrained to the horizontal plane; no vertical or torsional motion is incorporated into the model. The N-S and E-W motions are assumed to be independent. For convenience, let $\mathbf{x}(\mathbf{t})$ denote the N-S component of motion and $\mathbf{y}(\mathbf{t})$ denote the E-W component of displacement. The lumped model does not account for flexibility at the base; the base is assumed to be perfectly rigid. A state-space formulation is developed to numerically subject the model building to a pulse at its base.

A.5 State Space Formulation

The state of a system is a minimum set of numbers (state variables), which contain sufficient information about the history of the system or process to allow computation of future behavior (Timothy and Bona, 1968).

A.5.0.1 Differential Equations of Motion

The 23-degree-of-freedom lumped mass model is fixed at its base to the ground. Each mass in the model is approximated from the effective mass of the building floors, and is constrained to motion in the horizontal plane. Horizontal springs connect the masses, and their values are approximated from the effective inter-story shear stiffness. We first derive the state space formulation for the N-S direction. As the E-W motion is assumed to be independent, a similar set of equations can be reached by following the same derivation. The differential equations of motion are given by:

$$M\ddot{x}(t) + C\dot{x}(t) + Kx(t) = f(t), \tag{A.3}$$

where displacement vector $x(t)$ contains the generalized coordinates for the system, force vector $f(t)$ defined below in Equation A.7, and the mass, stiffness, and damping matrices (assuming Rayleigh damping) are given by:

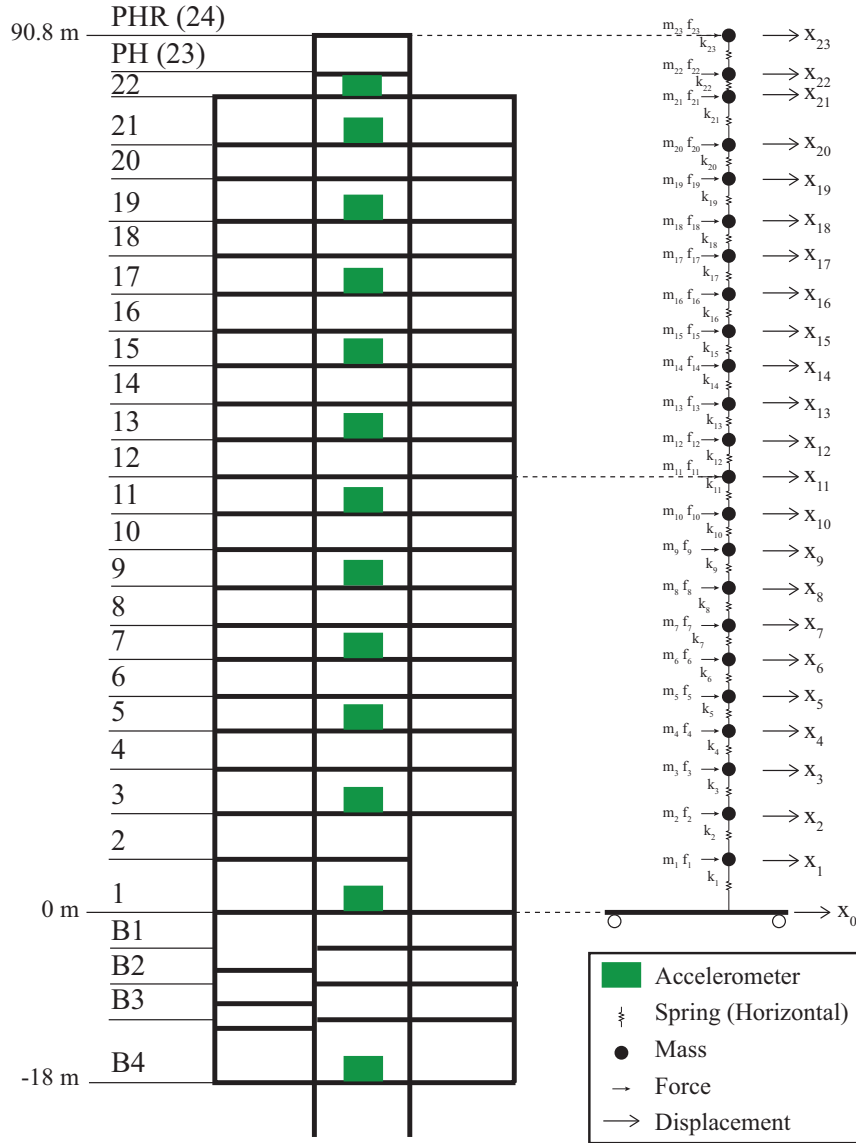


Figure A.5: **Osaka High-Rise: Building Schematic and Model**

The building is modeled as a 23-degree-of-freedom lumped mass system. It is densely instrumented with 13 seismometers located along the center of the building.

$$x(t) = \begin{pmatrix} x_1(t) \\ x_2(t) \\ \vdots \\ x_{23}(t) \end{pmatrix} \quad M = \begin{pmatrix} m_1 & 0 & \dots & 0 \\ 0 & m_2 & \dots & 0 \\ \vdots & \vdots & \ddots & \vdots \\ 0 & 0 & \dots & m_{23} \end{pmatrix},$$

$$K = \begin{pmatrix} k_1 + k_2 & -k_2 & 0 & \dots & 0 & 0 & 0 \\ -k_2 & k_2 + k_3 & -k_3 & \dots & 0 & 0 & 0 \\ 0 & -k_3 & k_3 + k_4 & \dots & 0 & 0 & 0 \\ \vdots & \vdots & \vdots & \ddots & \vdots & \vdots & \vdots \\ 0 & 0 & 0 & \dots & k_{21} + k_{22} & -k_{22} & 0 \\ 0 & 0 & 0 & \dots & -k_{22} & k_{22} + k_{23} & -k_{23} \\ 0 & 0 & 0 & \dots & 0 & -k_{23} & k_{23} \end{pmatrix} \quad C = \alpha K + \beta M.$$

These equations can be verified by drawing a free-body diagram for each mass in the mass-spring system. Ground motion is incorporated into the differential equations of motion by replacing it with an equivalent force, $f_0(t)$, applied to mass m_1 . There are contributions of $\alpha k_1 x_0$ and $\alpha k_1 \dot{x}_0$ to $f_0(t)$ from the first floor spring and the Rayleigh damper, respectively, that arise from their connection between mass m_1 and the ground. These contributions to the equivalent force can be verified by drawing a free body diagram for m_1 that includes the effects of Rayleigh damping; a schematic for Rayleigh damping can be found in Figure A.6.

$$f_{ext}(t) = \left(f_1(t) \quad f_2(t) \quad \dots \quad f_{23}(t) \right)^T, \quad (\text{A.4})$$

$$f_0(t) = k_1 x_0(t) + \alpha k_1 \dot{x}_0(t), \quad (\text{A.5})$$

$$B := \left(k_1 \quad 0 \quad \dots \quad 0 \right)^T, \quad (\text{A.6})$$

$$f(t) = Bx_0(t) + \alpha B\dot{x}_0(t) + f_{ext}(t). \quad (\text{A.7})$$

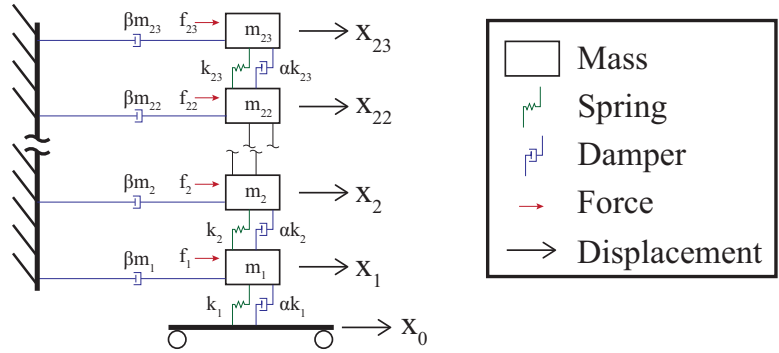


Figure A.6: **Mass-Spring System with Rayleigh Damping**

The model is represented as a mass-spring system with linear viscous damping that is consistent with Rayleigh damping. The contribution from the ground motion can be incorporated into the model as an equivalent force transmitted to the first floor mass via the damper and spring connecting the ground floor to the first floor.

A.5.0.2 Canonical Equations

A change of variables is introduced to transform from the generalized coordinates to the state vector, x_{state} , which contains the state variables, and from the force vector and ground motion to the input vector u . An output vector is denoted by y . The state vector and output vector can be rewritten as:

$$\begin{aligned} x_{state} &= f(x_{state}(t_0), u), \\ y &= g(x_{state}(t_0), u). \end{aligned}$$

A linear differential system characterized by the state equations of the canonical form:

$$\begin{aligned} \dot{x}_{state} &= Ax_{state} + Bu, \\ y &= Cx_{state} + Du, \end{aligned}$$

always has a unique solution for x_{state} .

Single Input System We first consider the case where the source consists purely of ground motion, i.e., $f_{ext}(t) = 0$. During events such as earthquakes, where the building response

is predominantly seismic, the external forces applied to the model contribute a negligible amount to building motion and can subsequently be ignored.

Introduce the state vector x_{state} , state variables $x_{1\ state}$ and $x_{2\ state}$, and input vector u as:

$$\begin{aligned} x_{state} &= \begin{pmatrix} x_{1\ state} & x_{2\ state} \end{pmatrix}^T, \\ x_{1\ state} &= x, \\ x_{2\ state} &= \dot{x} - \alpha M^{-1} B x_0, \\ u &= x_0. \end{aligned}$$

Note that the second term in the equation for $x_{2\ state}$ has been introduced to prevent the dependence of the state variables on \dot{u} . Rearranging Equation A.3, we find:

$$\ddot{x} - \alpha M^{-1} B \dot{x}_0 = M^{-1} B x_0 - M^{-1} C \dot{x} - M^{-1} K x.$$

The derivatives of the state variables can now be expressed in terms of the input and state variables:

$$\begin{aligned} \dot{x}_{1\ state} &= \dot{x} \\ &= x_{2\ state} + \alpha M^{-1} B x_0 \\ &= x_{2\ state} + \alpha M^{-1} B u, \\ \dot{x}_{2\ state} &= \ddot{x} - \alpha M^{-1} B \dot{x}_0 \\ &= M^{-1} B x_0 - M^{-1} C \dot{x} - M^{-1} K x \\ &= M^{-1} B u - M^{-1} C \dot{x}_{1\ state} - M^{-1} K x_{1\ state} \\ &= M^{-1} B u - M^{-1} C x_{2\ state} - \alpha M^{-1} C M^{-1} B u - M^{-1} K x_{1\ state}. \end{aligned}$$

Finally, the relation between the state variable and its derivative is expressed in matrix form:

$$\dot{x}_{state} = \begin{pmatrix} 0_{23 \times 23} & I_{23 \times 23} \\ -M^{-1} K & -M^{-1} C \end{pmatrix} x_{state} + \begin{pmatrix} \alpha M^{-1} B \\ (I - \alpha M^{-1} C) M^{-1} B \end{pmatrix} u. \quad (\text{A.8})$$

The system is now expressed in canonical form in Equation A.8. In the canonical state equations, Equations A.9a and A.9b,

$$\dot{x}_{state} = A_{state}x_{state} + B_{state}u, \quad (\text{A.9a})$$

$$y = C_{state}x_{state} + D_{state}u, \quad (\text{A.9b})$$

the matrices C_{state} and D_{state} are defined to give the desired output. For example, to output all of the model displacements, take $C_{state} = \begin{pmatrix} I & 0_{23 \times 23} \end{pmatrix}$ and $D_{state} = 0$. If there is a single output, the system is referred to as a SISO (single-input-single-output) system. If there are multiple outputs, the system is referred to as a SIMO (single-input-multiple-output) system. For our application, C_{state} is selected to output only the model displacements on floors with accelerometers.

Multiple Input System Consider the case where the source consists of an external force (e.g. wind loading) applied to each floor as well as ground motion at the base of the structure. The external forces have a larger impact on the motion of the building during ambient conditions than they do during seismic conditions. We follow the same derivation as in the previous section, while modifying the force vector, Equation A.5, to include the external forces:

$$\begin{aligned} f(t) &= \begin{pmatrix} f_1(t) \\ f_2(t) \\ \vdots \\ f_{23}(t) \end{pmatrix} + \begin{pmatrix} f_0(t) \\ 0 \\ \vdots \\ 0 \end{pmatrix} \\ &= f_{ext}(t) + Bx_0(t) + \alpha B\dot{x}_0(t). \end{aligned} \quad (\text{A.10})$$

The modified state variables are:

$$\begin{aligned}x_{1\ state} &= x, \\x_{2\ state} &= \dot{x} - \begin{pmatrix} \alpha M^{-1} B & 0_{23 \times 23} \end{pmatrix} \begin{pmatrix} x_0 \\ f_{ext} \end{pmatrix} \\u &= \begin{pmatrix} x_0 \\ f_{ext} \end{pmatrix}.\end{aligned}$$

Rearranging Equation A.3, we have:

$$\ddot{x} - \alpha M^{-1} B \dot{x}_0 = M^{-1} B x_0 + M^{-1} f_{ext} - M^{-1} C \dot{x} - M^{-1} K x.$$

The derivatives of the state variables are calculated to be:

$$\begin{aligned}\dot{x}_{1\ state} &= \dot{x} \\&= x_{2\ state} + \begin{pmatrix} \alpha M^{-1} B & 0_{23 \times 23} \end{pmatrix} \begin{pmatrix} x_0 \\ f_{ext} \end{pmatrix} \\&= x_{2\ state} + \begin{pmatrix} \alpha M^{-1} B & 0_{23 \times 23} \end{pmatrix} u, \\ \dot{x}_{2\ state} &= \ddot{x} - \alpha M^{-1} B \dot{x}_0 \\&= M^{-1} B x_0 + M^{-1} f_{ext} - M^{-1} C \dot{x} - M^{-1} K x \\&= \begin{pmatrix} M^{-1} B & M^{-1} \end{pmatrix} u - M^{-1} C \dot{x}_{1\ state} - M^{-1} K x_{1\ state} \\&= \begin{pmatrix} M^{-1} B & M^{-1} \end{pmatrix} u - M^{-1} C x_{2\ state} - \begin{pmatrix} \alpha M^{-1} C M^{-1} B & 0_{23 \times 23} \end{pmatrix} u - M^{-1} K x_{1\ state} \\&= \left((I - \alpha M^{-1} C) M^{-1} B \quad M^{-1} \right) u - M^{-1} C x_{2\ state} - M^{-1} K x_{1\ state}.\end{aligned}$$

And hence,

$$\dot{x}_{state} = \begin{pmatrix} 0_{23 \times 23} & I_{23 \times 23} \\ -M^{-1}K & -M^{-1}C \end{pmatrix} x_{state} + \begin{pmatrix} \alpha M^{-1}B & 0_{23 \times 23} \\ (I - \alpha M^{-1}C)M^{-1}B & M^{-1} \end{pmatrix} u. \quad (\text{A.11})$$

As there are multiple inputs to the system, x_0 , it is known as a multiple input system. If there is a single output, the system is referred to as a MISO (multiple-input-single-output) system. If there are multiple outputs, the system is referred to as a MIMO (multiple-input-multiple-output) system.

Alternate Formulation Using Principal Coordinates By converting to principal coordinates and reformulating the state space equations, the numerical accuracy of the solution can be improved. Let λ_n and ϕ_n , $n = 1, 2, \dots, 23$, denote the eigenvalues and normalized eigenvectors of $M^{-1}K$. Then $x(t)$ can be expressed in terms of the principal coordinates $p(t)$:

$$\begin{aligned} \lambda_n &= \omega_n^2 = (2\pi f_n)^2, \\ \Phi &= \begin{pmatrix} \phi_1 & \phi_2 & \dots & \phi_{23} \end{pmatrix}, \\ x(t) &= \Phi p(t), \\ p(t) &= \Phi^{-1}x(t), \\ \Phi^T K \Phi &= [\omega^2] = \begin{pmatrix} \omega_1^2 & 0 & \dots & 0 \\ 0 & \omega_2^2 & \dots & 0 \\ \vdots & \vdots & \ddots & \vdots \\ 0 & 0 & \dots & \omega_{23}^2 \end{pmatrix}, \\ \Phi^T M \Phi &= I. \end{aligned}$$

The differential equations of motion, Equation A.3, are uncoupled by expressing x in terms of the principal coordinates p and multiplying both sides of the equation by Φ^T :

$$\Phi^T M \Phi \ddot{p}(t) + \Phi^T C \Phi \dot{p}(t) + \Phi^T K \Phi p(t) = \Phi^T f(t),$$

$$\ddot{p}(t) + \Phi^T C \Phi \dot{p}(t) + \Phi^T K \Phi p(t) = \Phi^T f(t). \quad (\text{A.12})$$

Single-Input System

If we assume a single input, $x_0(t)$, then we can rewrite Equation A.12 as:

$$\ddot{p} - \alpha \Phi^T B \dot{x}_0 = \Phi^T B x_0 - \Phi^T C \Phi \dot{p} - \Phi^T K \Phi p.$$

The modified state variable is:

$$\begin{aligned} x_{1\text{state}} &= p, \\ x_{2\text{state}} &= \dot{p} - \alpha \Phi^T B x_0, \\ u &= x_0. \end{aligned}$$

By taking the derivatives of the state variables, we arrive at the state equation:

$$\dot{x}_{\text{state}} = \begin{pmatrix} 0_{23 \times 23} & I_{23 \times 23} \\ -\Phi^T K \Phi & -\Phi^T C \Phi \end{pmatrix} x_{\text{state}} + \begin{pmatrix} \alpha \Phi^T B \\ (I_{23 \times 23} - \alpha \Phi^T C \Phi) \Phi^T B \end{pmatrix} u. \quad (\text{A.13})$$

To output all of the model displacements, convert back to the original coordinates from the principal coordinates by taking $C_{\text{state}} = \begin{pmatrix} \Phi & 0_{23 \times 23} \end{pmatrix}$ and $D_{\text{state}} = 0$.

Multiple-Input System

If we assume multiple inputs $x_0(t)$ and $f_{\text{ext}}(t)$, then we can rewrite Equation A.12 as:

$$\ddot{p} - \alpha \Phi^T B \dot{x}_0 = \Phi^T B x_0 + \Phi^T f_{\text{ext}} - \Phi^T C \Phi \dot{p} - \Phi^T K \Phi p.$$

The state variable becomes:

$$\begin{aligned} x_{1\text{state}} &= p, \\ x_{2\text{state}} &= \dot{p} - \alpha \Phi^T B x_0, \\ u &= x_0. \end{aligned}$$

By taking the derivatives of the state variables, we arrive at the state equation:

$$\dot{x}_{state} = \begin{pmatrix} 0_{23 \times 23} & I_{23 \times 23} \\ -\Phi^T K \Phi & -\Phi^T C \Phi \end{pmatrix} \dot{x}_{state} + \begin{pmatrix} \alpha \Phi^T B & 0_{23 \times 23} \\ (I_{23 \times 23} - \alpha \Phi^T C \Phi) \Phi^T B & \Phi^T \end{pmatrix} u. \quad (\text{A.14})$$

To output all of the model displacements, convert back to the original coordinates from the principal coordinates by taking $C_{state} = \begin{pmatrix} \Phi & 0_{23 \times 23} \end{pmatrix}$ and $D_{state} = 0$.

State Space Coordinate Change and Transfer Function More generally, a coordinate change can be made for the state space system by introducing the transformation $\tilde{x} = Tx$, where T is a nonsingular matrix (Timothy and Bona, 1968). The state space matrices are also transformed. In the equations below, the subscript “state” has been dropped for convenience:

$$\begin{aligned} \tilde{A} &= TAT^{-1}, \\ \tilde{B} &= TB, \\ \tilde{C} &= CT^{-1}, \\ \tilde{D} &= D. \end{aligned}$$

The coefficient matrix A is transformed by what is known as a similarity transformation; the eigenvalues of the transformed matrix are the same as those of the original matrix. To convert back to the original state space coordinates, take $x = T^{-1}\tilde{x}$.

We can convert to a transfer function representation of the system by taking the Laplace transform of the state space equations. The transfer function $H(s)$ relates the output of the

model to the input. Assuming zero initial conditions, we find that:

$$\begin{aligned}
 sX(s) &= AX(s) + BU(s), \\
 X(s) &= (sI - A)^{-1}BU(s), \\
 Y(s) &= CX(s) + DU(s), \\
 &= (C(sI - A)^{-1}B + D)U(s).
 \end{aligned}$$

By considering a change of coordinates, we show that the transfer system remains the same for the new formulation. In changing from a state space representation with state variables defined by the generalized coordinates to a representation with state variables defined by the principal coordinates, as was done in the previous section, we were performing a transformation from one state space to another with $T = \Phi$.

$$\begin{aligned}
 H(s) &= \frac{Y(s)}{U(s)} \\
 &= C(sI - A)^{-1}B + D, \\
 \tilde{H}(s) &= \tilde{C}(sI - \tilde{A})^{-1}\tilde{B} + \tilde{D} \\
 &= CT^{-1}(sI - TAT^{-1})^{-1}TB + D \\
 &= CT^{-1}(T(sI - A)T^{-1})^{-1}TB + D \\
 &= CT^{-1}T(sI - A)^{-1}T^{-1}TB + D \\
 &= C(sI - A)^{-1}B + D \\
 &= H(s).
 \end{aligned}$$

Consider a state space formulation where $D = 0$, as it is the case for the lumped mass model. By rewriting the transfer function using the property that for an invertible matrix M , $M^{-1} = \text{adj}\{M\}/|M|$, where ‘adj’ stands for the adjugate matrix, the denominator of the transfer function can be in terms of the characteristic equation of A . Hence the poles of the

transfer functions are the eigenvalues of the matrix A :

$$\begin{aligned} H(s) &= \frac{Y(s)}{U(s)} \\ &= \frac{C \operatorname{adj}(sI - A) B}{|sI - A|}. \end{aligned}$$

A.5.0.3 State Space Solution

According to Ljung (1987), the general solution for the state vector $x_{state}(t)$ is given by:

$$x_{state}(t) = \Phi(t, t_0)x_{state}(t_0) + \int_{t_0}^t \Phi(t, \tau)B(\tau)u(\tau) d\tau,$$

where the state transition matrix $\Phi(t, t_0)$ is the unique solution to:

$$\begin{aligned} x_{state}(t) &= \Phi(t, t_0)x_{0\ state}, \\ \frac{d}{dt}\Phi(t, t_0) &= A(t)\Phi(t, t_0). \end{aligned}$$

Assuming zero initial conditions ($x_{0\ state} = 0$), an initial time of zero ($t_0 = 0$), and that the system is linear and time-invariant, the solution for $x_{state}(t)$ simplifies to:

$$\begin{aligned} \Phi(t, t_0) &= e^{A(t-t_0)}, \\ e^{At} &:= \sum_{k=0}^{\infty} \frac{A^k t^k}{k!}, \\ x_{state}(t) &= \int_0^t \Phi(t, \tau)Bu(\tau) d\tau \\ &= \int_0^t e^{A(t-\tau)}Bu(\tau) d\tau. \end{aligned}$$

This solution can be checked by hand by substituting it into Equation A.9a.

We can choose to numerically solve for x_{state} by computing the difference $x_{state}(t + \Delta t) - x_{state}(t)$, converting from a continuous system to a discrete system, and deriving a recurrence relation for x_{state} . Time step Δt is chosen so that the dynamics of the system are well-constrained (i.e., $\Delta t = \frac{T_{23}}{10}$, where T_N is the modal period of the highest considered mode N

of the model):

$$\begin{aligned}
x_{state}(t + \Delta t) &= \int_0^{t+\Delta t} e^{A(t+\Delta t-\tau)} Bu(\tau) d\tau \\
&= e^{A\Delta t} \int_0^t e^{A(t-\tau)} Bu(\tau) d\tau + \int_t^{t+\Delta t} e^{A(t+\Delta t-\tau)} Bu(\tau) d\tau \\
&= e^{A\Delta t} x_{state}(t) + \int_t^{t+\Delta t} e^{A(t+\Delta t-\tau)} Bu(\tau) d\tau \\
&\approx e^{A\Delta t} x_{state}(t) + \frac{\Delta t}{2} Bu(t + \Delta t) + \frac{\Delta t}{2} e^{A\Delta t} Bu(t).
\end{aligned}$$

In the last step, the trapezoidal rule was applied to approximate the integral $\int_t^{t+\Delta t} e^{A(t+\Delta t-\tau)} Bu(\tau) d\tau$. This step can also be worked out by hand to verify. If we denote $x_n = x_{state}(n\Delta t)$ and $u_n = u(n\Delta t)$, we end up with a recurrence relation for x_{state} :

$$x_{n+1} = e^{A\Delta t} x_n + \frac{\Delta t}{2} Bu_{n+1} + \frac{\Delta t}{2} e^{A\Delta t} Bu_n, \quad (\text{A.15})$$

$$q_n = Cx_n + Du_n. \quad (\text{A.16})$$

We can now numerically solve for x_{state} using Equation A.15, by starting at $n = 0$ and incrementally solving for x_1, x_2, \dots, x_N . Note that matrices A and B are defined in Equation A.8. Once we are done computing x_{state} , we use Equation A.16 to output the displacements in the generalized coordinates. It is also possible to solve for x_{state} in the frequency domain.

In Figure A.7, the state-space method was used to generate the impulse response functions to both an impulse applied at the ground floor, and to a force impulse applied at the 15th floor. Note that the force impulse imparts positive net momentum into the system, exciting the rocking response of the building. If the force were being applied inside the building, the net momentum introduced to the system would necessarily sum to zero. A sample frequency response function is shown in Figure A.8. The phase goes to zero near the natural frequency.

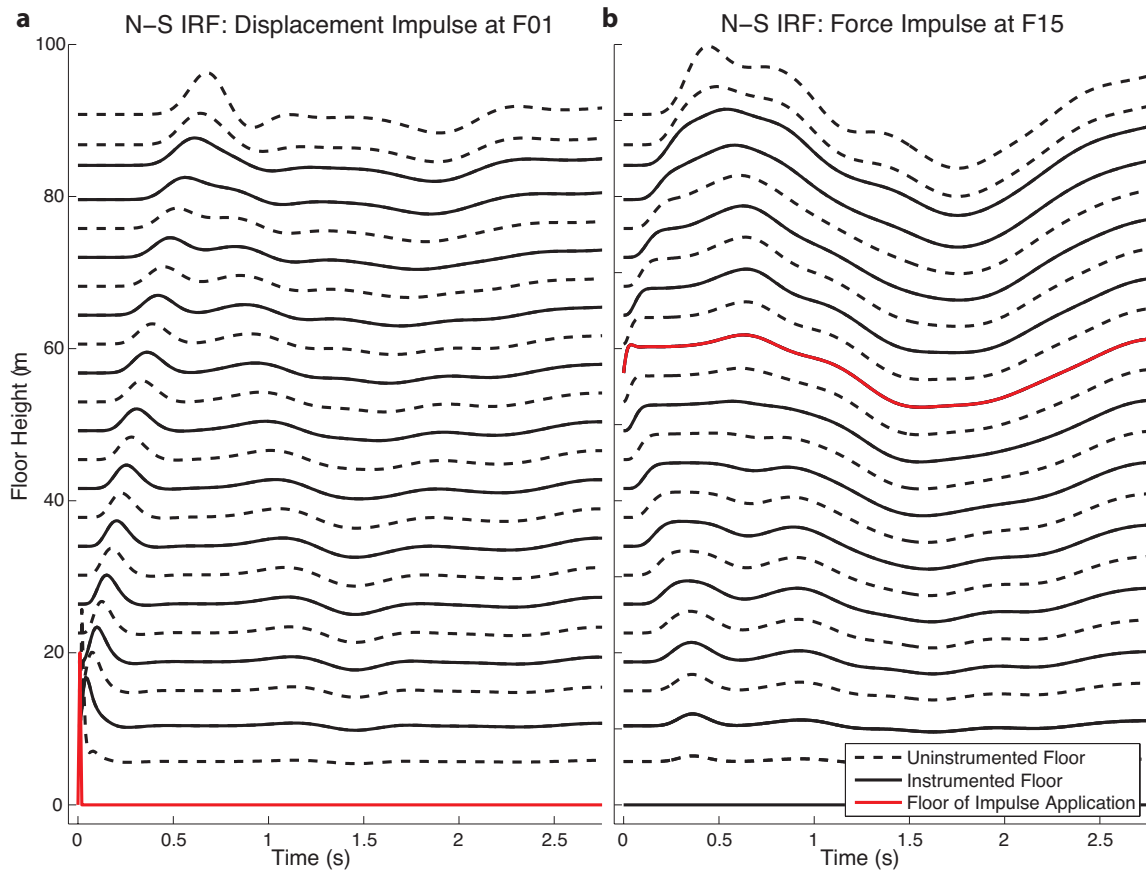


Figure A.7: **Numerical Impulse Response Functions.** The amplitude at each floor has been normalized proportionally to the maximum amplitude of the input floor, thus preserving the relative amplitudes. The floor to which the impulse is applied is highlighted in red. The numerical impulse response functions are calculated using the state space method with the design parameters for the N-S direction.

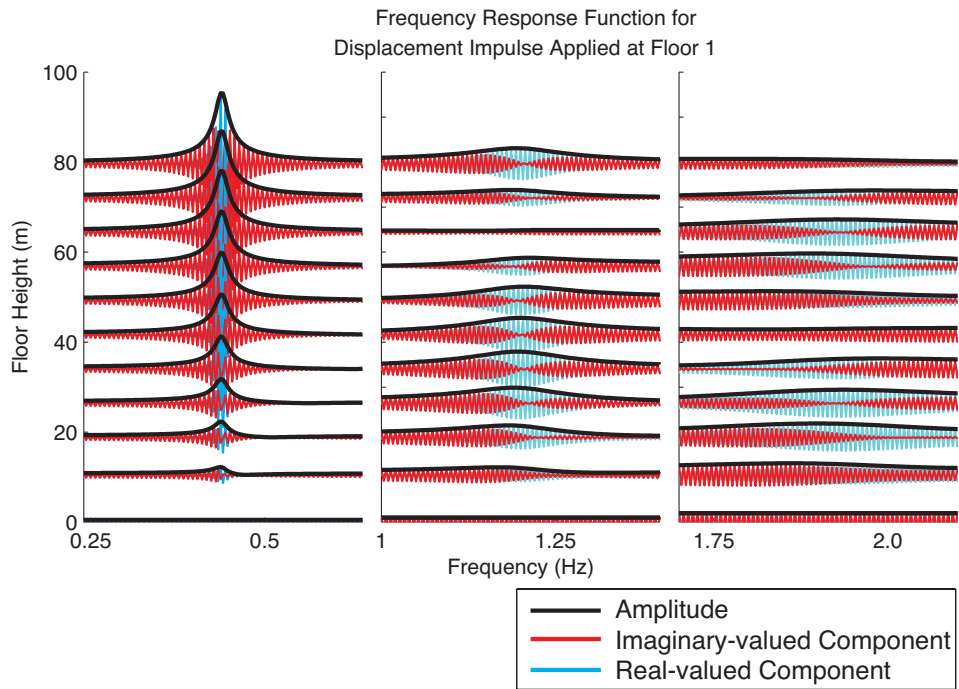


Figure A.8: **Numerical Frequency Response Function.** The frequency response function at the top floor in response to a displacement impulse applied at the first floor was calculated numerically by using the state-space method and the Fourier transform. The amplitude (black), imaginary component (red), and real component (blue) are shown for the first three N-S modes. The amplitudes have been normalized proportionally to the maximum amplitude of the input floor, thus preserving the relative amplitude.

A.5.1 Modal Analysis Using the Laplace Transform Method

We can alternatively use the Laplace transform method to solve for $x(t)$. Consider the uncoupled differential equation for the generalized coordinates, Equation A.12, and take the Laplace transform of each side. Assume zero initial conditions. Let $\zeta_n = (\alpha\omega_n + \beta/\omega_n)/2$ denote the n^{th} modal damping ratio. The damped natural frequency for the n^{th} mode is equal to $\omega_n\sqrt{1 - \zeta_n^2}$. Equation A.12 becomes:

$$(s^2I + s(\alpha[\omega^2] + \beta I) + [\omega^2])P(s) = \Phi^T F(s).$$

Converting back to generalized coordinates using the relation $X(s) = \Phi P(s)$, and inverting the diagonal matrix yields:

$$X(s) = \Phi \begin{pmatrix} (s^2 + 2\zeta_1\omega_1s + \omega_1^2)^{-1} & 0 & \dots & 0 \\ 0 & (s^2 + 2\zeta_2\omega_2s + \omega_2^2)^{-1} & \dots & 0 \\ \vdots & \vdots & \ddots & \vdots \\ 0 & 0 & \dots & (s^2 + 2\zeta_{23}\omega_{23}s + \omega_{23}^2)^{-1} \end{pmatrix} \Phi^T F(s).$$

Let us first consider the case with zero external forces, i.e., $f_{ext}(t) = 0$. Then the force acting on the system is equal to the equivalent force $f_0(t)$, given by Equation A.5, acting on the first floor mass m_1 . The equation for $X(s)$ simplifies to:

$$X(s) = k_1(1 + \alpha s) \begin{pmatrix} \sum_{p=1}^{23} \phi_p^1 \phi_p^1 (s^2 + 2\zeta_p\omega_p s + \omega_p^2)^{-1} \\ \sum_{p=1}^{23} \phi_p^1 \phi_p^2 (s^2 + 2\zeta_p\omega_p s + \omega_p^2)^{-1} \\ \vdots \\ \sum_{p=1}^{23} \phi_p^1 \phi_p^{23} (s^2 + 2\zeta_p\omega_p s + \omega_p^2)^{-1} \end{pmatrix} X_0(s).$$

This expression gives a vector of transfer functions multiplied by the transformed input ground motion, which is the equivalent of convolution of the impulse response function with the input in the time domain. The 46 distinct poles common to the transfer functions are

given by $\{-\omega_n(\zeta_n \pm i\sqrt{1-\zeta_n^2})\}$. The real parts of the poles are negative, consistent with a stable system. The transfer functions also have a common zero at $\frac{-1}{\alpha}$.

Let us now consider the case where the only source is a force applied at the m^{th} floor, i.e., $f_n(t) = 0 \forall n \neq m$, and $x_0(t) = 0$. Again, the result is given by a vector of transfer functions multiplied by the transformed input force $F_m(s)$. In the time domain, the solution is equivalent to a vector of convolutions of the impulse response functions with the input force. All transfer functions for the system have the same poles:

$$X(s) = \begin{pmatrix} \sum_{p=1}^{23} \phi_p^m \phi_p^1 (s^2 + 2\zeta_p \omega_p s + \omega_p^2)^{-1} \\ \sum_{p=1}^{23} \phi_p^m \phi_p^2 (s^2 + 2\zeta_p \omega_p s + \omega_p^2)^{-1} \\ \vdots \\ \sum_{p=1}^{23} \phi_p^m \phi_p^{23} (s^2 + 2i\zeta_p \omega_p s + \omega_p^2)^{-1} \end{pmatrix} F_m(s).$$

The transfer functions and impulse response functions are given by:

$$G_{n0}(s) = \sum_{p=1}^{23} \frac{k_1(1 + \alpha s)}{s^2 + 2\zeta_p \omega_p s + \omega_p^2}, \quad (\text{A.17})$$

$$G_{nm}(s) = \sum_{p=1}^{23} \frac{\phi_p^m \phi_p^n}{s^2 + 2\zeta_p \omega_p s + \omega_p^2}, \quad (\text{A.18})$$

$$\begin{aligned} g_{n0}(t) &= \sum_{p=1}^{23} \phi_p^1 \phi_p^n k_1 \mathcal{L}^{-1} \left\{ \frac{1 + \alpha s}{s^2 + 2\zeta_p \omega_p s + \omega_p^2} \right\} \\ &= \sum_{p=1}^{23} \frac{\phi_p^1 \phi_p^n k_1 e^{-\zeta_p \omega_p t}}{\omega_p \sqrt{1 - \zeta_p^2}} \left((1 + \alpha \zeta_p \omega_p) \sin(\omega_p \sqrt{1 - \zeta_p^2} t) - 2\alpha \omega_p \sqrt{1 - \zeta_p^2} \cos(\omega_p \sqrt{1 - \zeta_p^2} t) \right), \\ g_{nm}(t) &= \sum_{p=1}^{23} \phi_p^m \phi_p^n \mathcal{L}^{-1} \left\{ \frac{1}{s^2 + 2\zeta_p \omega_p s + \omega_p^2} \right\} \\ &= \sum_{p=1}^{23} \phi_p^1 \phi_p^n \frac{1}{\omega_p \sqrt{1 - \zeta_p^2}} e^{-\zeta_p \omega_p t} \sin(\omega_p \sqrt{1 - \zeta_p^2} t). \end{aligned} \quad (\text{A.19})$$

The inverse Laplace transforms are calculated using complex integration by considering a half-circle contour of a finite radius in the complex plane, taking the limits as the radius tends towards infinity, and applying the Cauchy Residue Theorem (Fokas, 2003).

The transfer functions $G_{n0}(s), G_{nm}(s)$ are expressed in terms of the Laplace variable $s = \sigma + i\omega$. The impulse response functions $\{g_{n0}(t), g_{nm}(t)\}$ are equal to the inverse Laplace transform of the transfer functions, and they give the response of system to an impulse. The frequency response functions $G_{n0}(i\omega) = \hat{g}_{n0}(\omega)$ and $G_{nm}(i\omega) = \hat{g}_{nm}(\omega)$ can be directly computed from the transfer functions by taking $s = i\omega$, and they are equal to the Fourier transform of the impulse response functions.

The solution to arbitrary inputs is given by the convolution integral with the impulse response functions:

$$x_n(t) = \int_{-\infty}^{\infty} g_{n0}(\tau)x_0(t + \tau)d\tau + \sum_{m=1}^{23} \int_{-\infty}^{\infty} g_{nm}(\tau)f_m(t + \tau)d\tau.$$

As convolution in the time domain is equivalent to multiplication in the frequency domain, the solution could alternatively be calculated by transforming the inputs to the frequency domain, multiplying the transformed inputs with the transfer functions, and taking the inverse transform of the resulting product:

$$x_n(t) = \mathcal{F}^{-1}\{\hat{g}_{n0}\hat{x}_0\} + \sum_{m=1}^{23} \mathcal{F}^{-1}\{\hat{g}_{nm}\hat{f}_m\}.$$

For a number of applications, calculating the solution in the frequency domain is much faster than calculating the solution in the time domain. For example, consider the convolution of two discrete time series of length N . The time-domain solution necessitates performing N multiplications in calculating the sum of the product of the two time series N times, a total of N^2 multiplications. The frequency-domain solution consists in performing N multiplications to calculate the product of the two transformed vectors, and performing two discrete Fourier transforms and two inverse Fourier transforms. As a fast Fourier transform requires $O(N \log N)$ operations, for large values of N , it is much faster to use a frequency domain solver.

A.5.2 Transfer Functions, Cross-Correlation, Convolution, and Deconvolution

There are three main techniques for obtaining the impulse response function of a system: cross-correlation, deconvolution, and cross-correlation with deconvolution. An investigation of error with each of these methods is presented below.

A.5.2.1 Transfer Functions

As seen in the previous section, the displacement at each floor of our model, $x_n(t)$, can be expressed as sum of convolutions of the impulse response functions with the ground motion and external forces. We are particularly interested in obtaining the set of impulse response functions relating the input displacement at the ground floor to the output displacement at above-ground floors $\{g_{0n}\}$ for $(n = 1, \dots, N_{dof})$, as we are interested in obtaining the seismic response of the structure. If, on the other hand, we were more interested in studying the effects of wind on the structure, we would be more interested in obtaining the set of impulse response functions relating the external force applied at each floor to the displacement $\{g_{nm}\}$ for $(n = 1, \dots, N_{dof})$ and $(m = 1, \dots, N_{dof})$. The displacement on each floor is given by:

$$x_n(t) = (g_{n0} * x_0)(t) + \sum_{m=1}^{N_f} (g_{nm} * f_m)(t). \quad (\text{A.20})$$

A.5.2.2 Cross-Correlation

Express the displacement at the n^{th} floor in terms of the impulse response functions and cross correlate it with the displacement at the ground floor to find:

$$\begin{aligned}
C_{0n}(t) &= (x_0 \star x_n)(t) & (A.21) \\
&= x_0 \star (g_{n0} \star x_0 + \sum_{m=1}^{N_f} g_{nm} \star f_m) \\
&= x_0(-) \star (g_{n0} \star x_0 + \sum_{m=1}^{N_f} g_{nm} \star f_m) \\
&= (x_0(-) \star x_0) \star g_{n0} + \sum_{m=1}^{N_f} (x_0(-) \star f_m) \star g_{nm} \\
&= (x_0 \star x_0) \star g_{n0} + \sum_{m=1}^{N_f} (x_0 \star f_m) \star g_{nm}.
\end{aligned}$$

The number of external forces in our model, N_f , equals 23. If the source consists of perfectly uncorrelated noise, such that $(x_0 \star x_0)(t) = N\sigma_0^2\delta(t)$ and $(x_0 \star f_m)(t) = 0$, then the cross-correlation between the ground floor displacement and the n^{th} floor displacement yields the relevant impulse response function multiplied by a constant. In this case, we can normalize $C_{0n}(t)$ by $N\sigma_0^2$ to recover the impulse response function:

$$\begin{aligned}
C_{0n}(t) &= \frac{(x_0 \star x_n)(t)}{N\sigma_0^2} & (A.22) \\
&= g_{n0}(t).
\end{aligned}$$

Note that in the above derivations, we cross-correlated displacement time series with displacement time series to uncover the impulse response functions. We could have instead cross-correlated acceleration time series with acceleration time series. In this case,

$$\begin{aligned}
C_{0n}(t) &= (\ddot{x}_0 \star \ddot{x}_n)(t) \\
&= (\ddot{x}_0 \star \ddot{x}_0) \star g_{n0} + \sum_{m=1}^M (\ddot{x}_0 \star \ddot{f}_m) \star g_{nm}.
\end{aligned}$$

If the source consists of perfectly uncorrelated noise, such that $(\ddot{x}_0 \star \ddot{x}_0)(t) = N\sigma_0^2\delta(t)$ and $(\ddot{x}_0 \star \ddot{f}_m)(t) = 0$, then we could again normalize by $N\sigma_0^2$ to uncover the impulse response function.

We introduce errors to the recorded displacement time series, such that $\tilde{x}_0(t) = x_0(t) + e_0(t)$ and $\tilde{x}_n(t) = x_n(t) + e_n(t)$, where the recorded displacements $\tilde{x}_0(t)$ and $\tilde{x}_n(t)$ are equal to the “true” displacements plus an error term. Assume the errors have zero mean. Then Equation A.22 becomes:

$$\begin{aligned}
C_{0n} &= \frac{\tilde{x}_0 \star \tilde{x}_n}{N\tilde{\sigma}_0^2} \\
&= \frac{1}{N\tilde{\sigma}_0^2} \left((x_0 \star x_0 + e_0 \star x_0) \star g_{n0} + \sum_{m=1}^{N_f} (x_0 \star f_m + e_0 \star f_m) \star g_{nm} + (x_0 \star e_n) + (e_0 \star e_n) \right), \\
\tilde{\sigma}_0^2 &= E[(\tilde{x}_0 - E[\tilde{x}_0])^2] \\
&= E[(x_0 + e_0 - E[x_0 + e_0])^2] \\
&= E[(x_0 + e_0 - E[x_0] - E[e_0])^2] \\
&= E[(x_0 + e_0)^2] \\
&= E[x_0^2 + e_0^2 + 2x_0e_0] \\
&= E[x_0^2] + E[e_0^2] + E[2x_0e_0] \\
&= \sigma_0^2 + \sigma_e^2 + 2Cov[x_0, e_0] \\
&= \sigma_0^2 \left(1 + \frac{\sigma_e^2 + 2Cov[x_0, e_0]}{\sigma_0^2} \right).
\end{aligned}$$

If the errors are uncorrelated to other errors, forces, and displacements, and $(\ddot{x}_0 \star \ddot{x}_0)(t) = N\sigma_0^2\delta(t)$, this simplifies to:

$$C_{0n} = \frac{1}{1 + \frac{\sigma_e^2}{\sigma_0^2}} g_{n0} + \frac{1}{N\sigma_0^2} \frac{1}{1 + \frac{\sigma_e^2}{\sigma_0^2}} \left(\sum_{m=1}^{N_f} (x_0 \star f_m) \star g_{nm} \right).$$

We see that in the case of an input error, cross-correlation does not recover the true amplitude of the impulse response function g_{n0} . Instead, its amplitude is reduced by the fraction $\frac{1}{1+\sigma_e^2/\sigma_0^2}$.

A.5.2.3 Deconvolution

Let D_{0n} denote the deconvolution of the displacement of the ground floor from the displacement at the n^{th} floor:

$$\begin{aligned}
D_{0n}(t) &= \mathcal{F}^{-1} \left\{ \frac{\hat{x}_n}{\hat{x}_0} \right\} \\
&= \mathcal{F}^{-1} \left\{ \frac{\hat{g}_{n0}\hat{x}_0 + \sum_{m=1}^{N_f} \hat{g}_{nm}\hat{f}_m}{\hat{x}_0} \right\} \\
&= \mathcal{F}^{-1} \left\{ \frac{\hat{x}_0}{\hat{x}_0} \hat{g}_{n0} + \sum_{m=1}^{N_f} \frac{\hat{f}_m}{\hat{x}_0} \hat{g}_{nm} \right\} \\
&= g_{n0}(t) + \sum_{m=1}^{N_f} \left(\mathcal{F}^{-1} \left\{ \frac{\hat{f}_m}{\hat{x}_0} \right\} * g_{nm} \right) (t).
\end{aligned} \tag{A.23}$$

If an error is added to the recorded displacement time series, Equation A.23 becomes:

$$\begin{aligned}
D_{0n}(t) &= \mathcal{F}^{-1} \left\{ \frac{\hat{x}_n}{\hat{x}_0} \right\} \\
&= \mathcal{F}^{-1} \left\{ \left(\hat{g}_{n0} + \sum_{m=1}^{N_f} \hat{g}_{nm} \frac{\hat{f}_m}{\hat{x}_0} + \frac{\hat{e}_n}{\hat{x}_0} \right) \frac{1}{1 + \frac{\hat{e}_0}{\hat{x}_0}} \right\}.
\end{aligned}$$

When the error is introduced, a term $\frac{\hat{e}_n}{\hat{x}_0}$ resulting from the added error e_n is added to the transfer function \hat{g}_{n0} . The transfer function is also multiplied by the term $\frac{\hat{e}_0}{\hat{x}_0}$, whose amplitude can be bounded by using the triangle inequality. Let us express the complex term $\frac{\hat{e}_0}{\hat{x}_0}$ in polar form as $re^{i\theta}$, with amplitude $r = r(\xi)$ and phase $\theta = \theta(\xi)$. Then we find that the fractional term is bound by the following:

$$\frac{1}{1 + \left| \frac{\hat{e}_0}{\hat{x}_0} \right|} \leq \left| \frac{1}{1 + \frac{\hat{e}_0}{\hat{x}_0}} \right| \leq \frac{1}{\left| 1 - \left| \frac{\hat{e}_0}{\hat{x}_0} \right| \right|}, \quad (\text{A.24})$$

$$\frac{1}{1 + r} \leq \left| \frac{1}{1 + \frac{\hat{e}_0}{\hat{x}_0}} \right| \leq \frac{1}{|1 - r|}, \quad (\text{A.25})$$

$$\arg \left\{ \frac{1}{1 + \frac{\hat{e}_0}{\hat{x}_0}} \right\} = \arg \left\{ \frac{1}{1 + r e^{i\theta}} \right\}. \quad (\text{A.26})$$

If $r \approx 0$, (i.e., a relatively small spectral input error \hat{e}_0 compared to \hat{x}_0 for a given frequency), then the recovered impulse response function is close to that of the true impulse response function, as the amplitude and phase of the fraction are close to one and zero, respectively. If $r \gg 1$, (i.e., a relatively large spectral input error \hat{e}_0 compared to \hat{x}_0 for a given frequency), then the amplitude of the recovered impulse response function will be reduced by a factor of about $\frac{\hat{x}_0}{\hat{e}_0}$, and its phase will change by a value of $-\theta$. If $r \approx 1$, then both the amplitude and phase of the recovered transfer function are highly variable and dependent on the phase θ .

A.5.2.4 Cross-Correlation with Deconvolution

Instead of normalizing cross-correlation C_{0n} in the time domain, as in Equation A.22, we can choose to normalize the cross-correlation in the frequency domain, technically combining cross-correlation with deconvolution. By doing so, we can relax the conditions on the type of the source, so that the source does not need to be flat in the frequency domain, merely broadband in the frequency range of interest, while still being uncorrelated with the other

noise sources. The cross-correlation becomes:

$$\begin{aligned}
C_{0n}(t) &= \mathcal{F}^{-1} \left\{ \frac{\overline{\hat{x}_0 \hat{x}_n}}{\overline{\hat{x}_0 \hat{x}_0}} \right\} \\
&= \mathcal{F}^{-1} \left\{ \frac{\hat{x}_0 (\hat{g}_{n0} \hat{x}_0 + \sum_{m=1}^{N_f} \hat{g}_{nm} \hat{f}_m)}{\overline{\hat{x}_0 \hat{x}_0}} \right\} \\
&= \mathcal{F}^{-1} \left\{ \frac{\overline{\hat{x}_0 \hat{x}_0}}{\overline{\hat{x}_0 \hat{x}_0}} \hat{g}_{n0} + \sum_{m=1}^{N_f} \frac{\overline{\hat{x}_0 \hat{f}_m}}{\overline{\hat{x}_0 \hat{x}_0}} \hat{g}_{nm} \right\} \\
&= g_{n0}(t) + \sum_{m=1}^{N_f} \mathcal{F}^{-1} \left\{ \frac{\overline{\hat{x}_0 \hat{f}_m}}{\overline{\hat{x}_0 \hat{x}_0}} \right\} * g_{nm}(t).
\end{aligned} \tag{A.27}$$

If the noise sources are uncorrelated, this recovers the impulse response function $g_{n0}(t)$, otherwise, there is some contribution from the other impulse response functions. Note that in this case, since we are effectively dividing out the effects of the source in the frequency domain, the source can consist of colored noise. In dividing by $\overline{\hat{x}_0(\xi) \hat{x}_0(\xi)}$, we have implicitly assumed that $\overline{\hat{x}_0(\xi) \hat{x}_0(\xi)} > 0$, i.e., broadband excitation is needed over the frequency range of interest. Signal conditioning techniques, such as waterleveling, can be employed to prevent dividing by zero in the frequency domain. These techniques are touched upon in the following section.

If we add an error to the recorded displacement time series, Equation A.27 becomes:

$$\begin{aligned}
C_{0n}(t) &= \mathcal{F}^{-1} \left\{ \frac{\overline{\hat{x}_0 \hat{x}_n}}{\overline{\hat{x}_0 \hat{x}_0}} \right\} \\
&= \mathcal{F}^{-1} \left\{ \left(\hat{g}_{n0} + \sum_{m=1}^{N_f} \frac{\hat{f}_m}{\hat{x}_0} \hat{g}_{nm} + \frac{\hat{e}_n}{\hat{x}_0} \right) \frac{1}{1 + \frac{\hat{e}_0}{\hat{x}_0}} \right\}.
\end{aligned}$$

Again, a spectral error term $\frac{\hat{e}_n}{\hat{x}_0}$ is added to the transfer function \hat{g}_{n0} , and the entire sum is multiplied by a factor of $\frac{1}{1 + \frac{\hat{e}_0}{\hat{x}_0}}$.

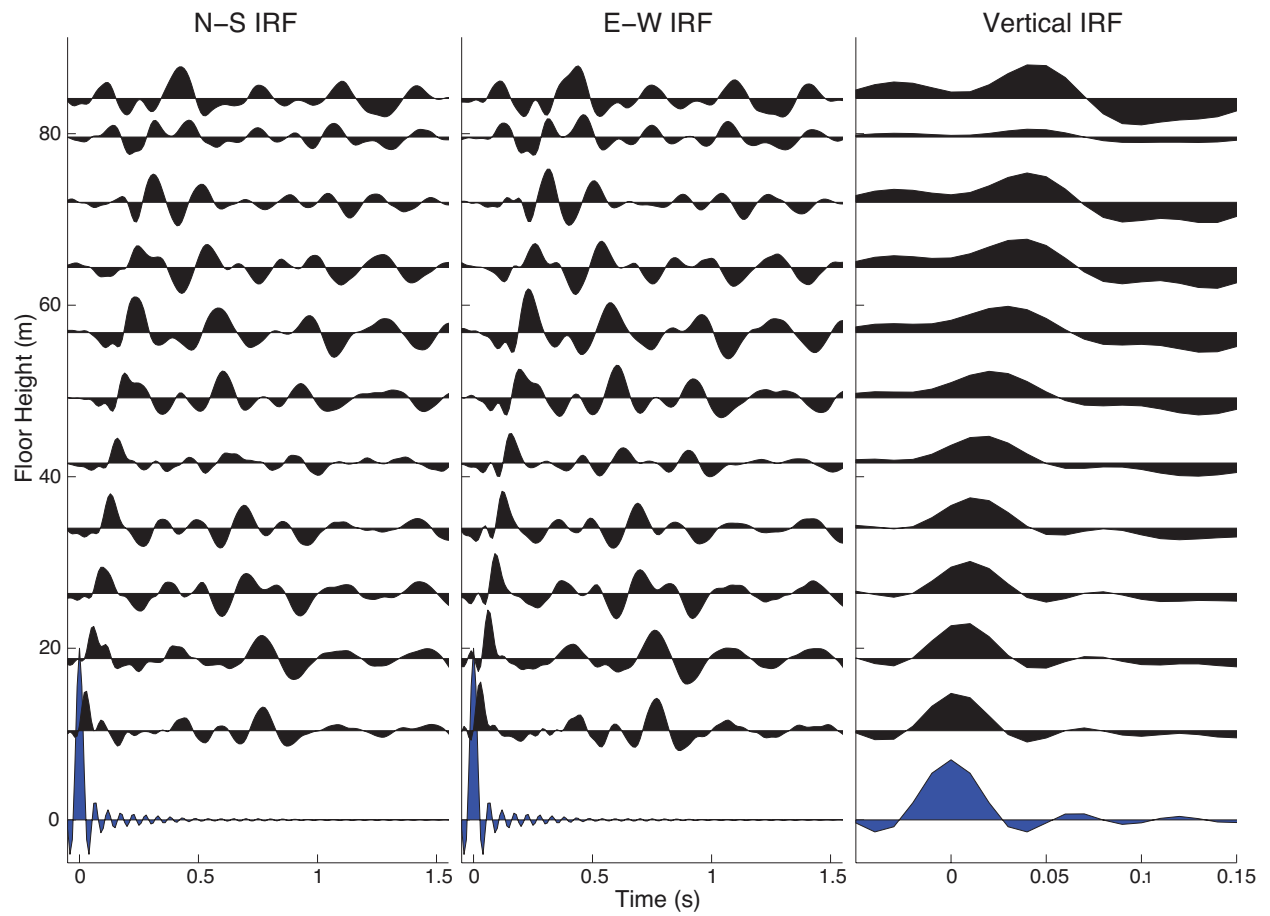


Figure A.9: **Experimental Impulse Response Functions.** The experimental impulse response functions were obtained by applying cross-correlation and convolution to an 8 hour segment of ambient data.

A.5.2.5 Experimental Results

The impulse response functions, shown in Figure A.9, were obtained experimentally by applying cross-correlation with deconvolution (Equation A.27) to an 8 hour segment of ambient data. This method was not observed to excite a strong torsional response (e.g., N-S motion generated by an E-W pulse at the base). The following signal conditioning techniques are employed to improve numerical stability and reduce artifacts:

Hamming Window The time series data is rescaled via a Hamming window before converting to the frequency domain. This is done in order to reduce artifacts that arise from taking the Fourier transform of a signal of finite duration. In this numerical study, the Hamming window is selected to be $0.2N_t$, where N_t is the length of the data. Only the first $0.1N_t$ and last $0.1N_t$ data points are scaled by the Hamming window.

Waterleveling Waterleveling is applied to the Fourier transformed data to prevent dividing by zero when division is performed in the frequency domain. Waterleveling is accomplished by replacing any values that have an absolute value less than a predefined “waterlevel” (chosen to be a fraction of the mean absolute value or max absolute value of the Fourier transformed data) with the phase-preserved waterlevel.

Clipping Clipping is applied to decrease the contribution of an earthquake or other large-amplitude event to a time series. Clipping can be applied either by rescaling a data point that is larger than a predefined amplitude while preserving the sign (or phase). In this sense, it is the opposite of waterleveling.

Whitening Whitening can be applied in either the time domain or the frequency domain to reduce the effect of an earthquake, or to artificially whiten a signal that has colored components. It is performed by rescaling each point inversely proportionally to the sum of amplitudes in a window centered at that point.

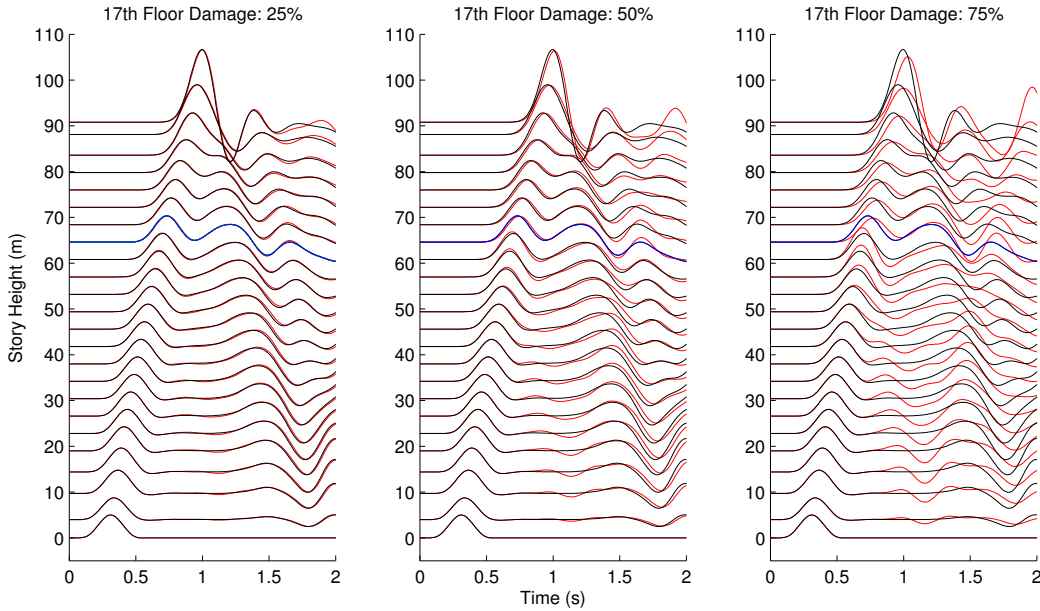


Figure A.10: **Numerically Computed IRFs.** Shear wave propagation in a damaged (red curves) and undamaged (black curves) numerical model of a high rise building. The blue curve indicates the damaged floor.

Filtering A filter (Butterworth) is applied to the resulting data to further separate the targeted signal.

A.5.3 Numerical Results:

Damaged vs. Undamaged Building

Damage is created in the numerical model by changing the stiffness between floors, with a reduction of 25% in interstory damage, 50% in interstory damage, and 75% in interstory damage, and only small changes in the IRF are observed. As the source consists of mostly low-frequency energy, as opposed to the shake table used for the experimental shear beam, damage detection based on detecting changes in the arrival time of the initial traveling wave generated in the estimated IRF is difficult. Hence, the frequency content and variable nature of the input signal limits the feasibility of this method for damage detection. Results from these simulated experiments indicate that a 30% reduction in single inter-story stiffness provides a measurable change in the amplification and transmission coefficients of the initial

pulse, and a 50% reduction in inter-story stiffness yields an observable change in the wave speed. The method is limited by the nature of the input signal, which tends to consist of lower-frequency energies and be variable over time.

Floor	Height	Weight	N-S Stiffness	E-W Stiffness	Model	Instrument
<i>PHR</i>	90.8	355080	1.442e8	1.500e8	x_{23}, y_{23}	—
<i>PHF</i>	86.8	331390	3.883e8	3.697e8	x_{22}, y_{22}	—
<i>F22</i>	84.1	879170	4.599e8	4.129e8	x_{21}, y_{21}	13
<i>F21</i>	79.6	699080	6.698e8	6.090e8	x_{20}, y_{20}	12
<i>F20</i>	75.8	717690	7.414e8	6.718e8	x_{19}, y_{19}	—
<i>F19</i>	72.0	717690	7.757e8	7.188e8	x_{18}, y_{18}	11
<i>F18</i>	68.2	717690	8.169e8	7.532e8	x_{17}, y_{17}	—
<i>F17</i>	64.4	717690	8.483e8	7.934e8	x_{16}, y_{16}	10
<i>F16</i>	60.6	717690	9.140e8	8.678e8	x_{15}, y_{15}	—
<i>F15</i>	56.8	717690	9.581e8	8.934e8	x_{14}, y_{14}	9
<i>F14</i>	53.0	717690	9.856e8	9.208e8	x_{13}, y_{13}	—
<i>F13</i>	49.2	717690	1.022e9	9.9601e8	x_{12}, y_{12}	8
<i>F12</i>	45.4	733900	1.049e9	1.010e9	x_{11}, y_{11}	—
<i>F11</i>	41.6	733900	1.071e9	1.042e9	x_{10}, y_{10}	7
<i>F10</i>	37.8	717690	1.158e9	1.136e9	x_9, y_9	—
<i>F09</i>	34.0	717690	1.147e9	1.164e9	x_8, y_8	6
<i>F08</i>	30.2	717690	1.139e9	1.194e9	x_7, y_7	—
<i>F07</i>	26.4	717690	1.155e9	1.224e9	x_6, y_6	5
<i>F06</i>	22.6	717690	1.204e9	1.274e9	x_5, y_5	—
<i>F05</i>	18.8	717690	1.320e9	1.360e9	x_4, y_4	4
<i>F04</i>	15.0	717690	1.325e9	1.357e9	x_3, y_3	—
<i>F03</i>	10.4	917750	1.278e9	1.251e9	x_2, y_2	3
<i>F02</i>	05.7	1042210	1.482e9	1.411e9	x_1, y_1	—
<i>F01</i>	00.0	362010	4.176e10	5.537e10	x_0, y_0	2
<i>B01</i>	−4.0	2606600	6.278e10	7.148e10	—	—
<i>B02</i>	−7.6	5878800	8.714e10	8.890e10	—	—
<i>B03</i>	−11.2	9170900	6.427e10	8.163	—	—
<i>B04</i>	−18	12802300	—	—	—	1

Table A.1: **Osaka High-Rise: Design Parameters.** The design parameters used in the model were obtained by Satow Architects, Design, and Engineers, based on the designed structure. The units are: height (m), weight (kg), stiffness (N/m).

A.6 Equipment List

Specifications	Value	Units
Sensor Supply Current	2-20, Adjustable	mA
Number of Sensor Channels	16	
Sensor Excitation Voltage (Compliance Voltage)	+24	VDC
Voltage Gain	UNITY	
Front Panel D'Arsonval Panel Meter		
F.S. DC Volts	+24	VDC
F.S. DC mA	20	mA
Output Coupling Capacitor (Each Channel)	10	μ F
Coupling Time Constant		
With 10 Megohm Load	9.0	SEC
With 1 Megohm Load	5.0	SEC
Lower -3db Frequency		
With 10 Megohm Load	0.017	Hz
With 1 Megohm Load	0.032	Hz
High Frequency Response	Determined by Sensor and Cable Length	
Noise, Wideband	150	μ V
Sensor Connectors, Rear Panel (16)	BNC	Jack
Output Connectors, Rear Panel (16)	BNC	Jack
Power Cord, 3-Wire with Chassis Ground	3-Wire Plug	6 ft
Power Required Model	13.0	VA
Line Voltage Required (standard model)	115	VAC 50-400 Hz
Line Voltage Required ('E' version)	230	VAC 50-400 Hz
Size, H x W x D	1.75 x 19.0 x 11.1	IN
Weight	5.0/2.3	Lbs./kG.

Table A.2: **Instrument Specifications: Accelerometer Power Rack.** Specifications for the Model 4116 sixteen-channel, rack-mounted power unit with adjustable sensor drive current.

Specifications	Value	Units
Physical		
Weight	3.8	grams
Size (Hex x Height)	.50 x .53	inches
Mounting Provision	10-32, UNF-2B	
Connector, Coaxial, Radially Mounted	10-32, UNF-2A	
Case Material	Anodized Alum.	
Connector Material	Stainless Steel	
Performance		
Sensitivity, +10%/-5% Measured at 100 Hz		
3150A5	500	mV/G
3150A3	100	mV/G
Range F.S. for +/- 4 Volts Out 3150A5	+/- 4	G's
Range F.S. for +/- 5 Volts Out 3150A3	+/- 50	G's
Frequency Response, +/- 5%	1-3000	Hz
Mounted Resonant Frequency, Nom.	8 (12)	kHz
Phase Response, +/- 5 Degrees Phase Shift	1-3000	Hz
Equivalent Electrical Noise (Resolution)	.0001	G, RMS
Transverse Sensitivity, Max.	5	Percent
Strain Sensitivity	.001	G, RMS
Amplitude Non-linearity (Zero Based Best Fit St. Line Method)	2.0	% F.S., Max
Transverse Sensitivity, Max.	5	Percent
Strain Sensitivity	.001	250 G's/ $\mu\sigma$
Environmental		
Maximum Vibration	50	G's, RMS
Maximum Shock	1000	G's, Peak
Temperature Range	-60 to +250	degF
Thermal Coefficient of Sensitivity	0.1	% / deg F
Electrical		
Excitation (Compliance) Voltage Range	+20 to + 30	VDC
Excitation Current Range	2 to 20	mA
Output Impedance, Nom.	100	OHMS
Output Bias Voltage, +/- Volt	12	VDC
Discharge Time Constant, Min.	1	VDC
Output Signal Polarity for Acceleration Toward Top	Positive Going	

Table A.3: **Instrument Specifications: Accelerometer.** Specifications for the Model 3150A3 and 31250A5 high-sensitivity, low-mass LIVM accelerometer.

Specifications	Value	Units
Dynamic Performance		
Voltage Sensitivity	100	mV/g
Measurement Range	50	±g pk
Frequency Range		
±5%	1-4000	Hz
±10%	0.7-7000	Hz
±3 dB	0.35-12000	Hz
Mounted Resonant Frequency	≥22	kHz
Resolution - Broadband	0.001	g pk
Amplitude Linearity	%	±1
Transverse Sensitivity	%	≤5
Environmental		
Shock Limit (Maximum)	10000	±g pk
Operating Temperature Range	-65 to +250	degF
Strain Sensitivity	≤0.0002	g/μϵ
Electrical		
Excitation Voltage/Constant Current	18-30/2-20	VDC/mA
Output Impedance	<100	ohms
Output Bias	8-12	VDC
Discharge Time Constant	≥0.5	sec
Warm Up Time (within 10% of output bias)	45	μV rms
Broadband Electrical Noise (1-10 kHz)	45	μV rms
Spectral Noise		
1 Hz	320	μg/√Hz
10 Hz	70	μg/√Hz
100 Hz	18	μg/√Hz
1 kHz	6.4	μg/√Hz
Ground Isolation	None (Optional)	ohms
Mechanical		
Sensing Element	Quartz/Shear	Material/Geometry
Housing	Titanium	Material
Housing	Welded Hermetic	Sealing
Size (hex x height)	0.75 x 0.85	inch
Weight	0.88	oz
Electrical Connector	10-32 Coaxial/Side	Type/Location
Mounting Thread	10-32 Female	Size

Table A.4: **Instrument Specifications: Hammer.** Specifications for the Quartz Shear ICP accelerometer used in the force-transducer hammer.

Model No.		482A	482A04
Specification	Units	Value	Value
Supply Voltage	+V	24	24/Channel
Excitation Current (Constant Current Source)	mA	2-20	2-20/Channel
Coupling Capacitor	μ F	10	10
DC Offset (Max) (w/1 Megohm Load at "Scope" Output)	mV	30	30
Output Noise, Wideband, Pk-Pk (Max)	μ F	300	300
Voltage Gain		1:1	1:1
Fault Monitor Meter	V/FS	24	24
Power Required (40 to 400 Hz)	V/A	105 to 125/.12	105 to 125/.12
Power Cord (3-Wire)	ft	6	6
Connectors:			
Input (XDCR) (Microdot)	THD	10-32	10-32
Output (Scope)	Jack	BNC	BNC
Size (H x W x D)	in	4.3 x 1.8 x 6.0	4.3 x 1.8 x 6.0
Weight	lbs	2	2

Table A.5: **Instrument Specifications: Hammer Power Unit.** Specifications for the PCB Piezotronics ICP line power unit.

Specification	Value
Analog Input	
Channels	32, 16
Single-Ended Channels	32
Differential Channels	16
Resolution	16 bits
Sample Rate	2 MS/s
Throughput (All Channels)	1 MS/s
Max Voltage	10 V
Maximum Voltage Range	-10 V, 10 V
Minimum Voltage Range	-0.1 V, 0.1 V
Number of Ranges	7
Simultaneous Sampling	No
Analog Output	
Channels	4
Resolution	16 bits
Max Voltage	10 V
Maximum Voltage Range	-10 V, 10 V
Minimum Voltage Range	-5 V, 5 V
Update Rate	2.86 MS/s
Current Drive Single	5 mA
Digital I/O	
Bidirectional Channels	48
Input-Only Channels	0
Output-Only Channels	0
Timing	Software, Hardware
Clocked Lines	32
Maximum Clock Rate	1 MHz
Logic Levels	TTL
Input Current Flow	Sinking, Sourcing
Output Current Flow	Sinking, Sourcing
Programmable Input Filters	Yes
Supports Programmable Power-Up States?	Yes
Current Drive Single	24 mA
Current Drive All	1 A

Table A.6: **Instrument Specifications: Data Acquisition System.** Specifications for the National Instruments NI USB-6363 X Series multifunction data acquisition.

Bibliography

- Aagaard, B., Williams, C., and Knepley, M. (2008). PyLith: A finite-element code for modeling quasi-static and dynamic crustal deformation. In *AGU Fall Meeting Abstracts*, page 1925, San Francisco, CA.
- Aagaard, B. T., Knepley, M. G., and Williams, C. A. (2013). A domain decomposition approach to implementing fault slip in finite-element models of quasi-static and dynamic crustal deformation. *Journal of Geophysical Research: Solid Earth*, 118(6):3059–3079.
- Aktan, A., Catbas, F., Grimmelsman, K., and Tsikos, C. (2000). Issues in infrastructure health monitoring for management. *Journal of Engineering Mechanics*, 126(7):711–724.
- Allemang, R. J. (2003). The modal assurance criterion (MAC): Twenty years of use and abuse. *Sound and Vibration Magazine*, 37(8):14–21.
- Anstey, N. A. (1964). Correlation techniques - A review. *Geophysical Prospecting*, 12(4):355–382.
- Astroza, M., Ruiz, S., and Astroza, R. (2012). Damage assessment and seismic intensity analysis of the 2010 (M_w 8.8) Maule earthquake. *Earthquake Spectra*, 28(S1):S145–S164.
- ATC (2002). *Rapid Visual Screening of Buildings for Potential Seismic Hazards: A Handbook (FEMA 154)*. Applied Technology Council, Federal Emergency Management Agency, National Earthquake Hazards Reduction Program, 2nd Edition.
- Atwater, B. F. and Hemphill-Haley, E. (1997). *Recurrence intervals for great earthquakes*

- of the past 3,500 years at northeastern Willapa Bay, Washington.* U.S. Geological Survey Professional Paper 1576.
- Bernal, D. and Beck, J. (2004). Preface to the special issue on Phase I of the IASC-ASCE structural health monitoring benchmark. *Journal of Engineering Mechanics*, 130(1):1–2.
- Bernal, D. and Gunes, B. (2004). Flexibility based approach for damage characterization: Benchmark application. *Journal of Engineering Mechanics*, 130(1):61–70.
- Binzel, R. P. (2000). The Torino impact hazard scale. *Planetary and Space Science*, 48(4):297–303.
- Black, C. and Ventura, C. (1998). Blind test on damage detection of a steel frame structure. In *Proceedings of the 16th International Modal Analysis Conference*, pages 623–629. Society for Experimental Mechanics, Inc.
- Boashash, B. (2003). *Time Frequency Signal Analysis and Processing: A Comprehensive Reference*. Elsevier, 1st Edition.
- Bornn, L., Farrar, C. R., and Park, G. (2010). Damage detection in initially nonlinear systems. *International Journal of Engineering Science*, 48(10):909–920.
- Bracewell, R. N. (1986). *The Fourier Transform and its Applications*. McGraw-Hill New York.
- Brincker, R., Zhang, L., and Andersen, P. (2000). Modal identification from ambient responses using frequency domain decomposition. In *Proceedings of the 8th International Modal Analysis Conference*, pages 625–630.
- Brockenbrough, R. and Merritt, F. (2006). *Structural Steel Designers Handbook: AISC, AASHTO, AISI, ASTM, AREMA, and ASCE-07 Design Standards*. American Society of Civil Engineers, 4th Edition.

- BSSC (2003). *NEHRP Recommended Provisions for Seismic Regulations for New Buildings and Other Structures (FEMA 450)*. Building Seismic Safety Council, National Institute of Building Sciences, Washington, D.C.
- Caicedo, J. M., Dyke, S. J., and Johnson, E. A. (2004). Natural excitation technique and eigensystem realization algorithm for Phase I of the IASC-ASCE benchmark problem: Simulated data. *Journal of Engineering Mechanics*, 130(1):49–60.
- Cheney, E. E. W. and Kincaid, D. R. (2012). *Numerical Mathematics and Computing*. Cengage Learning.
- Cheung, S. H. and Beck, J. L. (2009). Bayesian model updating using hybrid Monte Carlo simulation with application to structural dynamic models with many uncertain parameters. *Journal of Engineering Mechanics*, 135(4):243–255.
- Ching, J. and Beck, J. (2004). Bayesian analysis of the Phase II IASC-ASCE structural health monitoring experimental benchmark data. *Journal of Engineering Mechanics*, 130(10):1233–1244.
- Cole, H. A. (1971). *Method and Apparatus for Measuring the Damping Characteristics of a Structure*. U.S. Patent No. 3620069 A, U.S. Patent and Trademark Office.
- CSSC (1994). *A Compendium of Background Reports on the Northridge Earthquake*. California Seismic Safety Commission, Sacramento, CA.
- DesRoches, R., Comerio, M., Eberhard, M., Mooney, W., and Rix, G. J. (2011). Overview of the 2010 Haiti earthquake. *Earthquake Spectra*, 27(S1):S1–S21.
- Doebling, S., Farrar, C., Prime, M., and Shevitz, D. (1996). *Damage Identification and Health Monitoring of Structural and Mechanical Systems from Changes in their Vibration Characteristics: A Literature Review*. LANL Report LA-13070-MS. Los Alamos National Laboratory.

- Doebling, S. W., Farrar, C. R., and Prime, M. B. (1998). A summary review of vibration-based damage identification methods. *Shock and Vibration Digest*, 30(2):91–105.
- Dyke, S. J., Bernal, D., Beck, J., and Ventura, C. (2003). Experimental Phase II of the structural health monitoring benchmark problem. In *Proceedings of the 16th ASCE Engineering Mechanics Conference*.
- Eguchi, R. T., Goltz, J. D., Taylor, C. E., Chang, S. E., Flores, P. J., Johnson, L. A., Seligson, H. A., and Blais, N. C. (1998). Direct economic losses in the Northridge earthquake: A three-year post-event perspective. *Earthquake Spectra*, 14(2):245–264.
- Engelhardt, M. D. and Sabol, T. A. (1997). Seismic-resistant steel moment connections: Developments since the 1994 Northridge earthquake. *Progress in Structural Engineering and Materials*, 1(1):68–77.
- Ewins, D. J. (1984). *Modal Testing: Theory and Practice*. Research Studies Press, Letchworth.
- Ewins, D. J. (2000). Model validation: Correlation for updating. *Sadhana*, 25(3):221–234.
- Farrar, C. R., Worden, K., Todd, M. D., Park, G., Nichols, J., Adams, D. E., Bement, M. T., and Farinholt, K. (2007). *Nonlinear system identification for damage detection*. LANL Report LA-14353. Los Alamos National Laboratory.
- FEMA (2000). *State of the Art Report on Connection Performance (FEMA-355D)*. SAC Joint Venture, Federal Emergency Management Agency.
- FEMA (2007). *Welded Steel Moment Frame (Disaster Assistance Policy 9524.1)*. Federal Emergency Management Agency.
- Field, E. H., Dawson, T. E., Felzer, K. R., Frankel, A. D., Gupta, V., Jordan, T. H., Parsons, T., Petersen, M. D., Stein, R. S., and Weldon, R. (2009). Uniform California earthquake rupture forecast, Version 2 (UCERF 2). *Bulletin of the Seismological Society of America*, (4):2053–2107.

- Figueiredo, E. and Flynn, E. (2009). *Three-Story Building Structure to Detect Nonlinear Effects*. LANL Technical Report. Los Alamos National Laboratory.
- Figueiredo, E., Park, G., Farrar, C. R., Worden, K., and Figueiras, J. (2011). Machine learning algorithms for damage detection under operational and environmental variability. *Structural Health Monitoring*, 10(6):559–572.
- Figueiredo, E., Park, G., Figueiras, J., Farrar, C., and Worden, K. (2009). *Structural health monitoring algorithm comparisons using standard data sets*. LANL Report LA-14393. Los Alamos National Laboratory.
- Fink, M. (1992). Time reversal of ultrasonic fields - Part I: Basic principles. *IEEE Transactions on Ultrasonics, Ferroelectrics, and Frequency Control*, 39(5):555–566.
- Fokas, A. S. (2003). *Complex Variables: Introduction and Applications*. Cambridge University Press.
- Friswell, M. I. (2007). Damage identification using inverse methods. *Philosophical Transactions of the Royal Society A: Mathematical, Physical and Engineering Sciences*, 365(1851):393–410.
- Gibbons, S. and Ringdal, F. (2006). The detection of low magnitude seismic events using array-based waveform correlation. *Geophysical Journal International*, 165(1):149–166.
- Giurgiutiu, V. and Cuc, A. (2005). Embedded non-destructive evaluation for structural health monitoring, damage detection, and failure prevention. *Shock and Vibration Digest*, 37(2):83–105.
- Goldfinger, C., Nelson, C. H., Morey, A., Johnson, J. E., Gutierrez-Pastor, J., Eriksson, A. T., Karabanov, E., Patton, J., Garcia, E., and Enkin, R. (2012). *Turbidite event history: Methods and implications for Holocene paleoseismicity of the Cascadia subduction zone*. U.S.G.S. Professional Paper 1661F. U.S. Geological Survey.

- Gutenberg, B. and Richter, C. F. (1965). *Seismicity of the Earth and Associated Phenomena*. Hafner New York.
- Haiti (2010). *Action Plan for National Recovery and Development of Haiti*. Government of the Republic of Haiti.
- Hall, J. F., Schmid, B., Comerio, M., Russell, J., Quadri, N. D., Harder, R., Powell, B., Hamburger, R., and Steinberg, R. (1996). Wood buildings. *Earthquake Spectra*, 12(S1):125–176.
- Hamburger, R. O., Krawinkler, H., Malley, J. O., and Adan, S. M. (2009). *Seismic Design of Steel Special Moment Frames: A Guide for Practicing Engineers*. National Earthquake Hazards Reduction Program Seismic Design Technical Brief No. 2 (NIST GCR 09-917-3). National Institute of Standards and Technology, U.S. Department of Commerce.
- Hayashi, Y., Sugino, M., Yamada, M., Takiyama, N., Onishi, Y., and Akazawa, T. (2012). Consecutive vibration characteristics monitoring of high-rise steel building. In *Proceedings of STESSA 2012: The 7th International Conference on Behaviour of Steel Structures in Seismic Areas*, pages 1065–1070.
- Heaton, T. H. and Hartzell, S. H. (1987). Earthquake hazards on the Cascadia subduction zone. *Science*, 236(4798):162–168.
- Heckman, V., Kohler, M., and Heaton, T. (2010). Detecting failure events in buildings: A numerical and experimental analysis. In *Proceedings of the 9th U.S. National and 10th Canadian Conference on Earthquake Engineering*. Earthquake Engineering Research Institute.
- Heckman, V., Kohler, M., and Heaton, T. (2011a). A damage detection method for instrumented civil structures using prerecorded greens functions and cross-correlation. In *Proceedings of ANCRiSST2011: The 6th International Workshop on Advanced Smart Materials and Smart Structures Technology*.

- Heckman, V. M., Kohler, M. D., and Heaton, T. H. (2011b). A method to detect structural damage using high-frequency seismograms. In *Proceedings of Structural Health Monitoring 2011: International Workshop on Structural Health Monitoring*.
- Heckman, V. M., Kohler, M. D., and Heaton, T. H. (2011c). A method to detect structural damage using high-frequency seismograms. In *Proceedings of the 8th International Conference on Urban Earthquake Engineering*.
- Hera, A. and Hou, Z. (2004). Application of wavelet approach for ASCE structural health monitoring benchmark studies. *Journal of Engineering Mechanics*, 130(1):96–104.
- Hernandez-Garcia, M. R., Masri, S. F., Ghanem, R., Figueiredo, E., and Farrar, C. R. (2010). A structural decomposition approach for detecting, locating, and quantifying nonlinearities in chainlike systems. *Structural Control and Health Monitoring*, 17(7):761–777.
- ICC (2000). *2000 International Building Code*. International Code Council, Inc., U.S.A.
- Jennings, P. C. (2013). Earthquakes and engineers: An international history. *Earthquake Spectra*, 29(2):669–673.
- Johnson, E., Lam, H., Katafygiotis, L., and Beck, J. (2004). Phase I IASC-ASCE structural health monitoring benchmark problem using simulated data. *Journal of Engineering Mechanics*, 130(1):3–15.
- Juang, J.-N. and Pappa, R. S. (1985). An eigensystem realization algorithm for modal parameter identification and model reduction. *Journal of Guidance, Control, and Dynamics*, 8(5):620–627.
- Karaiskos, G., Tondreau, G., Figueiredo, E., Farrar, C., and Deraemaeker, A. (2012). Application of modal filters for damage detection in the presence of non-linearities. In *Proceedings of the 6th European Workshop on Structural Health Monitoring*.
- Kaufmann, E., Fisher, J., DiJulio, R., and Gross, J. (1997). *Failure Analysis of Welded Steel Moment Frames Damaged in the Northridge Earthquake (NISTIR 5944)*. Building and

Fire Research Laboratory, National Institute of Standards and Technology, Gaithersburg, MD.

- Kohler, M., Heaton, T., and Bradford, S. (2007). Propagating waves in the steel, moment-frame Factor building recorded during earthquakes. *Bulletin of the Seismological Society of America*, 97(4):1334–1345.
- Kohler, M. D., Heaton, T. H., and Heckman, V. M. (2009). A time-reversed reciprocal method for detecting high-frequency events in civil structures with accelerometer arrays. In *Proceedings of ANCRISST 2009 - The Fifth International Workshop on Advanced Smart Structures and Technology*.
- Krawinkler, H., Anderson, J., Bertero, V., Holmes, W., and Theil Jr, C. (1996). Steel buildings. *Earthquake Spectra*, 12(S1):25–47.
- Lam, H., Katafygiotis, L., and Mickleborough, N. (2004). Application of a statistical model updating approach on Phase I of the IASC-ASCE structural health monitoring benchmark study. *Journal of Engineering Mechanics*, 130(1):34–48.
- Li, H., Li, S., Ou, J., and Li, H. (2010). Modal identification of bridges under varying environmental conditions: Temperature and wind effects. *Structural Control and Health Monitoring*, 17(5):495–512.
- Li, H., Li, S., Ou, J., and Li, H. (2012). Reliability assessment of cable-stayed bridges based on structural health monitoring techniques. *Structure and Infrastructure Engineering*, 8(9):829–845.
- Li, S., Li, H., Liu, Y., Lan, C., Zhou, W., and Ou, J. (2013). SMC structural health monitoring benchmark problem using monitored data from an actual cable-stayed bridge. *Structural Control and Health Monitoring*.
- Ljung, L. (1987). *System Identification: Theory for the User*. Prentice-Hall Information and System Sciences Series. Prentice Hall, Englewood Cliffs, New Jersey.

- Lus, H., Betti, R., Yu, J., and De Angelis, M. (2004). Investigation of a system identification methodology in the context of the ASCE benchmark problem. *Journal of Engineering Mechanics*, 130(1):71–84.
- Marwala, T. (2010). *Finite-Element-Model Updating Using Computational Intelligence Techniques: Applications to Structural Dynamics*. Springer.
- Moehle, J. P. and Frost, J. D. (2012). Preface: Special issue on the 2010 Maule, Chile, earthquake. *Earthquake Spectra*, 28(S1):vii–viii.
- Moore, W. H. (2013). *National Transportation Statistics*. Bureau of Transportation Statistics, Research and Innovative Technology Administration, U.S. Department of Transport.
- Osteraas, J., Somers, P., Carpenter, J., Ferner, H., Holmes, W., Krawinkler, H., Longstreth, M., Ryan, P., and Wight, J. (1996). Reinforced concrete buildings. *Earthquake Spectra*, 12(S1):49–74.
- Park, H., Sohn, H., Law, K., and Farrar, C. (2007). Time reversal active sensing for health monitoring of a composite plate. *Journal of Sound and Vibration*, 302(1-2):50–66.
- Park, J., Song, T.-R. A., Tromp, J., Okal, E., Stein, S., Rault, G., Clevede, E., Laske, G., Kanamori, H., and Davis, P. (2005). Earth’s free oscillations excited by the 26 December 2004 Sumatra-Andaman earthquake. *Science*, 308(5725):1139–1144.
- Park, S., Stubbs, N., and Bolton, R. (1998). Damage detection on a steel frame using simulated modal data. In *Proceedings of the 16th International Modal Analysis Conference*, pages 616–622. Society for Experimental Mechanics, Inc.
- Petersen, M. D., Frankel, A. D., Harmsen, S. C., Mueller, C. S., Haller, K. M., Wheeler, R. L., Wesson, R. L., Zeng, Y., Boyd, O. S., and Perkins, D. M. (2008). *Documentation for the 2008 Update of the United States National Seismic Hazard Maps*. U.S.G.S. Open-File Report 2008-1128. U.S. Geological Survey.

- Prieto, G. A., Lawrence, J. F., Chung, A. I., and Kohler, M. D. (2010). Impulse response of civil structures from ambient noise analysis. *Bulletin of the Seismological Society of America*, 100(5A):2322–2328.
- Raghavan, A. and Cesnik, C. E. (2007). Review of guided-wave structural health monitoring. *Shock and Vibration Digest*, 39(2):91–116.
- Reitherman, R. K. (2012). *Earthquakes and Engineers: An International History*. American Society of Civil Engineers, Reston, VA.
- Rodgers, J., Mahin, S., and Celebi, M. (2007). Proposed approaches to fracture damage detection for sparsely instrumented steel moment-framed buildings. *International Journal of Steel Structures*, 7(1):1–10.
- Rodgers, J. E. and Mahin, S. A. (2007). Transient response in steel moment frames caused by brittle connection fracture. *Earthquake Engineering and Structural Dynamics*, 36(15):2423–2444.
- Rytter, A. (1993). *Vibrational Based Inspection of Civil Engineering Structures*. PhD thesis, University of Aalborg.
- SAC (2000). *Recommended Postearthquake Evaluation and Repair Criteria for Welded Steel Moment-Frame Buildings (FEMA-352)*. SAC Joint Venture, Federal Emergency Management Agency.
- Sagan, C., Druyan, A., and Soter, S. (1980). *Heaven and Hell*. Cosmos. KCET, Carl Sagan Productions, in association with British Broadcasting Corporation, Polytel International.
- Sasani, M., Makris, N., and Bolt, B. A. (2006). Damping in shear beam structures and estimation of drift response. *ASCE Journal of Engineering Mechanics*, 132(8):851–858.
- Satow (1962). *Sakai City New Building Construction Work*, Volume 2-4. Satow Engineers and Architects, Tokyo, Japan.

- Sharifi, A. and Banan, M. R. (2008). Energy index method: Technique for identification of structural damages. *Journal of Structural Engineering*, 134(6):1061–1064.
- Sohn, H., Farrar, C. R., Hemez, F. M., Shunk, D. D., Stinemates, D. W., Nadler, B. R., and Czarnecki, J. J. (2004). *A Review of Structural Health Monitoring Literature: 1996-2001*. LANL Technical Report. Los Alamos National Laboratory.
- Somers, P., Campi, D., Holmes, W., Kehoe, B. E., Klingner, R. E., Lizundia, B., and Schmid, B. (1996). Unreinforced masonry buildings. *Earthquake Spectra*, 12(S1):195–217.
- SSC (2004). *Status of the Unreinforced Masonry Building Law*. 2003 Report to the Legislature. Seismic Safety Commission, Sacramento, CA.
- Thatcher, W., Marshall, G., and Lisowski, M. (1997). Resolution of fault slip along the 470-km-long rupture of the great 1906 San Francisco earthquake and its implications. *Journal of Geophysical Research*, 102(B3):5353–5367.
- Timoshenko, S. (1951). *Theory of Elasticity*. Engineering Societies Monographs. McGraw-Hill New York, 2nd Edition.
- Timothy, L. K. and Bona, B. E. (1968). *State Space Analysis: An Introduction*. McGraw-Hill New York.
- Tromp, J., Tape, C., and Liu, Q. (2005). Seismic tomography, adjoint methods, time reversal and banana-doughnut kernels. *Geophysical Journal International*, 160(1):195–216.
- Udike, R. (1996). *USGS Response to an Urban Earthquake - Northridge '94*. U.S.G.S. Open-File Report 96-263. U.S. Geological Survey.
- USGS (2012). *Largest Earthquakes in the World Since 1900*. http://earthquake.usgs.gov/earthquakes/world/10_largest_world.php, November 30, 2012 16:21:34 UTC.

- Wald, D. J., Kanamori, H., Helmberger, D. V., and Heaton, T. H. (1993). Source study of the 1906 San Francisco earthquake. *Bulletin of the Seismological Society of America*, 83(4):981–1019.
- Wang, C., Rose, J., and Chang, F. (2004). A synthetic time-reversal imaging method for structural health monitoring. *Smart Materials and Structures*, 13(2):415–423.
- Wang, C. and Rose, L. (2003). Wave reflection and transmission in beams containing delamination and inhomogeneity. *Journal of Sound and Vibration*, 264(4):851–872.
- Wilson, E. L. (2004). *Static and Dynamic Analysis of Structures*. Computers and Structures, Inc., Berkeley, CA, 4th Edition.
- Wu, J. and Li, Q. (2006). Structural parameter identification and damage detection for a steel structure using a two-stage finite element model updating method. *Journal of Constructional Steel Research*, 62(3):231–239.
- Yang, J. N., Lei, Y., Lin, S., and Huang, N. (2004). Hilbert-Huang based approach for structural damage detection. *Journal of Engineering Mechanics*, 130(1):85–95.
- Youssef, N. F., Bonowitz, D., and Gross, J. L. (1995). *A Survey of Steel Moment-Resisting Frame Buildings Affected by the 1994 Northridge Earthquake (NISTIR 5625)*. Building and Fire Research Laboratory, National Institute of Standards and Technology, Gaithersburg, MD.
- Yuen, K.-V., Au, S. K., and Beck, J. L. (2004). Two-stage structural health monitoring approach for Phase I benchmark studies. *Journal of Engineering Mechanics*, 130(1):16–33.
- Zhao, B., Taucer, F., and Rossetto, T. (2009). Field investigation on the performance of building structures during the 12 May 2008 Wenchuan earthquake in China. *Engineering Structures*, 31(8):1707–1723.